

POLITECNICO DI TORINO

MASTER DEGREE THESIS

Department of Control and Computer Engineering

Mechatronic Engineering

*a.y. 2023/2024*

./svg-inkscape/Logo\_Polito\_svg-tex.pdf

# **Study of flexible PCB coils in haptic applications**

*Supervisors:*

Alessandro RIZZO  
(*Politecnico di Torino - DET*)

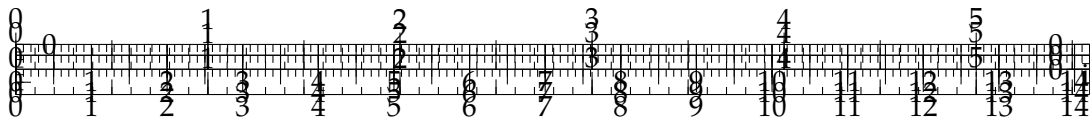
Domenico PRATTICHIZZO  
(*Università di Siena - DIISM - SIRSLab*)

Leonardo FRANCO  
(*Università di Siena - DIISM - SIRSLab*)

*Candidate:*

Morgan CASALE

April 2024



POLITECNICO DI TORINO

## *Abstract*

Department of Control and Computer Engineering  
Mechatronic Engineering

### **Study of flexible PCB coils in haptic applications**

by Morgan CASALE

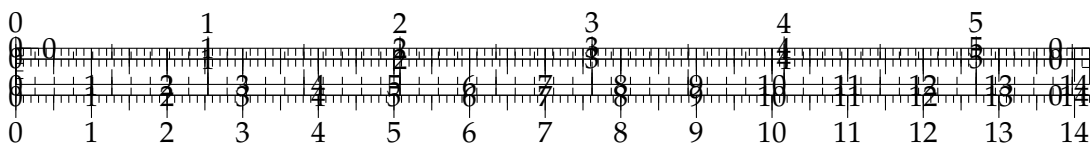
As the number of in-orbit satellites increases, the need for a way to service them becomes increasingly critical.

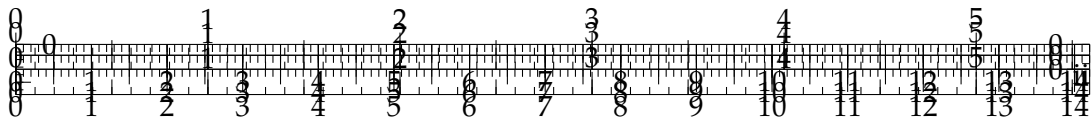
Recently the EU funded EROSS, a project with the purpose of providing a new range of services for in orbit satellites with consequent analysis for satellite design and life-cycle management. This initiative aims to enhance the availability of cost-effective and secure orbital services by assessing and validating the essential technological components of the Servicer spacecraft. The incorporation of robotic space technologies working on this project will lead to greater autonomy and safety in executing these services in space, requiring reduced ground-based supervision.

This master's thesis presents an innovative approach to pose estimation using deep learning and computer vision techniques. The research explores the development and implementation of a system for in-orbit satellites pose estimation. Delving into the complexities of rendezvous maneuvers, the system devised herein addresses the challenges associated with achieving and maintaining accurate pose estimations in the ever-changing and demanding conditions of space. Through a comprehensive exploration, this thesis contributes valuable insights and practical solutions to enhance the reliability and efficiency of satellite rendezvous processes.

A mono camera system is employed, reducing the hardware complexity and costs while maintaining performance. The camera captures pictures of the target satellite during the whole approach phase. A deep learning framework, based on a Convolutional Neural Network (CNN), is used to identify and track landmark features on the target satellite from captured images. This CNN-based approach provides high accuracy in feature recognition and tracking precision. A neural network-based regression model is introduced to map the 2D image coordinates of identified landmarks to their corresponding 3D coordinates with respect to the camera frame. This implementation permits to have a mono-camera instead of a stereo-camera system. Finally, incorporating the CPD algorithm, the system aligns the predicted 3D point clouds to the reference model, enabling accurate pose estimation and tracking.

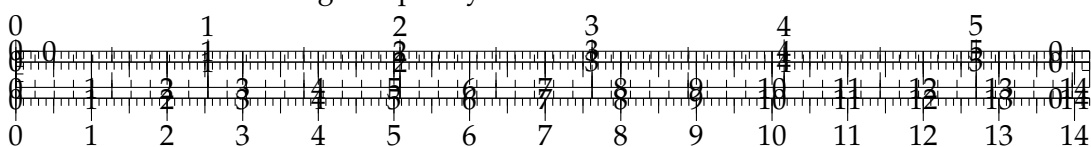
The proposed system is tested through simulations. The results demonstrate the system's capability to estimate the pose of in-orbit satellites. This research contributes to the advancement of autonomous satellite operations, space debris management, and space exploration. Furthermore, it has the potential to enhance satellite rendezvous and capture capabilities.

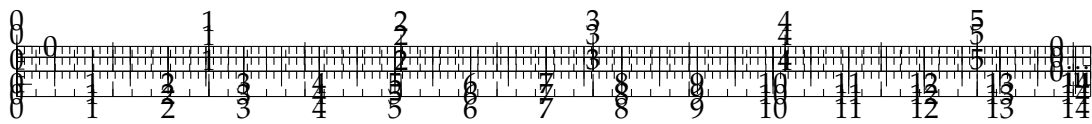




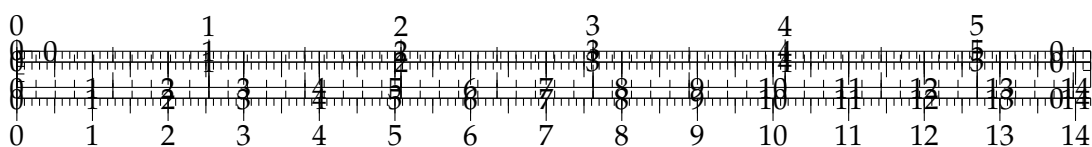
# Contents

<b>Abstract</b>	<b>i</b>
<b>1 Introduction</b>	<b>1</b>
1.1 Thesis objective . . . . .	1
1.2 Necessary background (?) . . . . .	2
1.3 Thesis structure . . . . .	4
<b>2 Background</b>	<b>6</b>
2.1 Magnetic Coils . . . . .	6
2.1.1 Brief History . . . . .	6
2.1.2 Physics of an inductor? . . . . .	6
Inductance . . . . .	6
Reactance . . . . .	7
Joule heating . . . . .	8
Definition of Root Mean Square (RMS) values . . . . .	8
2.1.3 Magnetic field generation . . . . .	8
Magnetic Flux and Field relation . . . . .	10
2.2 PCB Coils . . . . .	10
2.2.1 Planar coils . . . . .	11
2.2.2 Planar coil magnetic field . . . . .	12
2.2.3 Multi-layer PCB coils . . . . .	13
Total inductance . . . . .	13
Magnetic field generated by a Multilayer coil . . . . .	14
2.3 Flexible PCB coils . . . . .	14
2.3.1 Pros of flexible coils . . . . .	14
2.3.2 Application challenges . . . . .	15
Rise of high resistance . . . . .	15
Joule effect . . . . .	16
Magnetic field strength . . . . .	17
Resistance parasitic effects due to AC current . . . . .	18
2.3.3 Running flexible PCB coils . . . . .	21
High current needs . . . . .	21
Constant Voltage vs Constant Current power supplying . . . . .	23
2.4 Modelling of the Entire System . . . . .	23
2.4.1 Neodymium magnets (magnetic strength wrt class and dimensions) . . . . .	23
2.4.2 Magnetic force between magnet and coil . . . . .	24
2.4.3 Membrane-magnet system . . . . .	25
Membrane stiffness . . . . .	26
Membrane damping . . . . .	28
2.4.4 Finger grasping model . . . . .	29
2.5 Membrane-Finger haptic system . . . . .	29

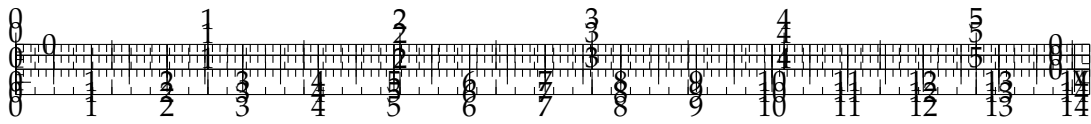




2.5.1	Introduction on haptic feedback . . . . .	29
2.5.2	Transfer of Energy between membrane and finger . . . . .	29
2.5.3	Magnetic strenght and Kinetic Energy . . . . .	29
<b>3</b>	<b>Overview of Haptic Feedback</b>	<b>31</b>
3.1	Introduction to Haptic Feedback . . . . .	31
3.1.1	Vibration Propagation in the finger's pulp . . . . .	31
3.2	Piezoelectric actuators . . . . .	31
3.2.1	Force performances . . . . .	31
3.2.2	Frequency response . . . . .	31
3.2.3	Powering circuits . . . . .	32
3.2.4	WeArt implementation . . . . .	32
3.3	Performance comparison between Piezo and Coil's actuators . . . . .	37
<b>4</b>	<b>Powering circuit design</b>	<b>38</b>
4.0.1	Power Circuit Block diagram . . . . .	38
4.1	Controller . . . . .	38
4.1.1	ESP32 waveform generator for a single module . . . . .	38
	Controller code . . . . .	38
	Esp32 DAC limitations . . . . .	38
	Esp32 DAC Noise . . . . .	38
4.2	Signal Conditioning Circuit . . . . .	43
4.3	Amplifier circuit . . . . .	43
4.3.1	High Power Operational Amplifiers . . . . .	43
	An old type of op-amp . . . . .	44
	Power dissipation problems . . . . .	44
4.3.2	High Power Voltage Amplifier . . . . .	44
4.4	Power Supply . . . . .	45
4.5	Implementation problems and possible alternatives . . . . .	45
4.5.1	Non idealities . . . . .	45
	Stability . . . . .	45
	Phase Shift . . . . .	45
	Noise . . . . .	45
	Slew-Rate . . . . .	45
4.5.2	Alternative Amplifiers . . . . .	45
	Current Amplifiers . . . . .	46
<b>5</b>	<b>Implementation and Prototypes</b>	<b>47</b>
5.1	Coils alternatives . . . . .	47
5.1.1	Dresda coils . . . . .	47
	Low magnetic field strenght . . . . .	47
	Fragility and low flexibility . . . . .	47
	Very high resistance and power needs . . . . .	47
5.1.2	Flexar coils . . . . .	47
	Higher magnetic field strenght . . . . .	47
	Higher flexibility . . . . .	47
	Lower resistance and power needs . . . . .	47
5.2	Rigid Prototypes . . . . .	47
5.2.1	1st version - Dresda Coils testbed . . . . .	47
	Dresda Coils . . . . .	47
	Flexible magnetic membrane . . . . .	47

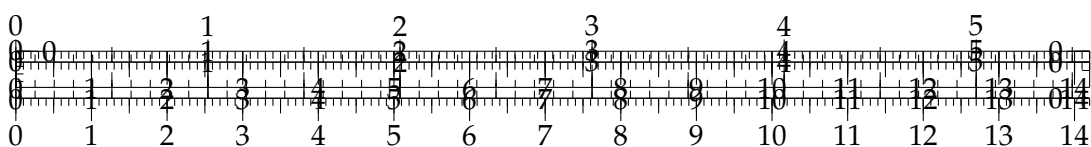


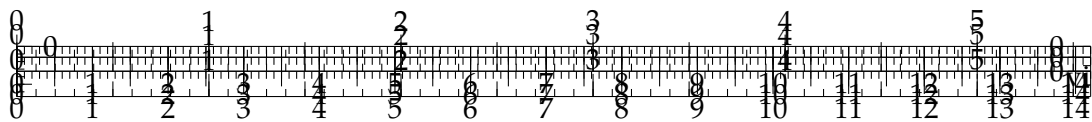
	Adjustable height platform for coil and membrane . . . . .	47
5.2.2	Wearable Rigid Prototypes . . . . .	47
	Finger-Membrane interface . . . . .	47
	Keep the distance from the coil . . . . .	48
	Heat dissipation . . . . .	48
5.3	Flexible Mat Prototypes . . . . .	49
5.3.1	Design of the membrane . . . . .	49
	Material stiffness and thickness . . . . .	49
	Membrane structure vs magnet dimensions . . . . .	49
5.3.2	Design of the mat . . . . .	49
	Distance magnet-coil . . . . .	49
	Coil trap . . . . .	49
	Production method and structure . . . . .	49
5.3.3	Design faults and problems . . . . .	49
	Membrane fragility . . . . .	49
	Overall system flexibility . . . . .	49
	Keeping the distance coil-magnet under finger pressure . . . .	49
	Production method . . . . .	49
5.4	Experimentation and Evaluation . . . . .	49
5.4.1	Heating testing . . . . .	51
	Single coil in DC . . . . .	51
	Single coil in AC [-V, V] . . . . .	52
	Single coil in AC [0, 2V] . . . . .	57
	Two coils in parallel DC . . . . .	60
	Two coils in parallel AC . . . . .	60
5.4.2	Magnet size vs Force . . . . .	61
5.4.3	Force vs number of coils . . . . .	67
5.4.4	Voltage vs Force . . . . .	67
6	Discussion and conclusions . . . . .	68
6.1	Challenges in On-Board AI Systems for Space Missions . . . . .	68
6.1.1	Verifiability Issues . . . . .	68
6.1.2	Computational Issues . . . . .	68
6.2	Results Analysis . . . . .	69
6.3	Possible Improvements . . . . .	69
6.3.1	Landmark Selection . . . . .	69
6.3.2	Landmark Mapping Sensitivity . . . . .	69
6.4	Conclusions . . . . .	70
A	Support Code . . . . .	71
A.1	Ground Truth Heatmaps . . . . .	71
A.2	Landmark Location Selection . . . . .	72
	Bibliography . . . . .	73
	Acknowledgements . . . . .	76



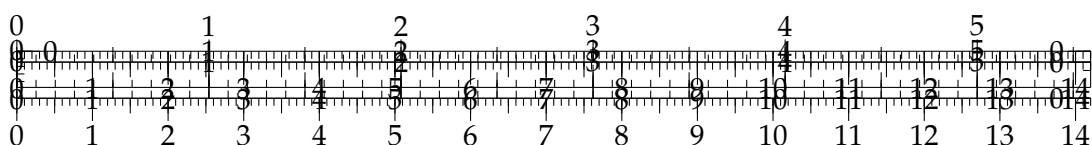
# List of Figures

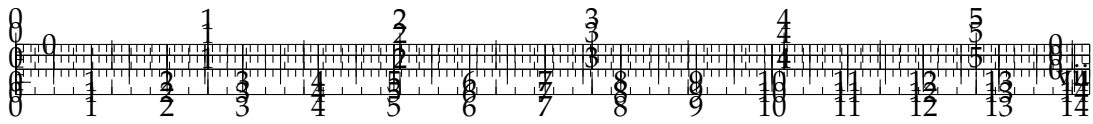
1.1	Sample images from <i>TASI EROSS IOD Simulated Dataset N°2</i> . . . . .	2
1.2	Model's UPS . . . . .	3
2.1	RMS values for different waveforms. . . . .	9
2.2	Coils Shapes . . . . .	11
2.3	Spiral magn field . . . . .	12
2.4	Coil spiral . . . . .	13
2.5	Skin depth . . . . .	19
2.6	Fskin of Flexar . . . . .	20
2.7	Skin effect on thicker traces . . . . .	20
2.8	Proximity effect . . . . .	21
2.9	Power Op Amp block diagram. . . . .	22
2.10	Power op-amp schematic . . . . .	22
2.11	Bond graph of the coil-magnet-membrane system. . . . .	23
2.12	Coil-Magnet position . . . . .	24
2.13	Coil-Magnet Transducer bond graph. . . . .	26
2.14	Membrane structure . . . . .	26
2.15	Membrane mat . . . . .	27
2.16	Bond graph of the membrane-magnet system. . . . .	27
2.17	Membrane arms parallel springs. . . . .	28
2.18	Final mechanical bond-graph of the membrane and magnet. . . . .	28
2.19	Model of two soft fingers grasping the object. . . . .	29
2.20	Bond graph of the finger grasping model. . . . .	30
3.1	HRNet . . . . .	34
3.2	Exchange Unit . . . . .	35
4.1	Offline pipeline . . . . .	38
4.2	CAD Model . . . . .	38
4.3	Landmark Identification Algorithm. . . . .	41
4.4	Landmarks identified by the Landmark Regression module. . . . .	41
4.5	Online pipeline of the implemented pose estimator. . . . .	43
4.6	Bilateral Filter. . . . .	43
4.7	Input and pre-processed image. . . . .	44
4.8	Iterations of the CPD optimization process. . . . .	45
5.1	2D error over the training dataset. . . . .	51
5.2	Landmark Regression error over the trajectory range. . . . .	51
5.3	Models Distribution . . . . .	53
5.4	Landmark Mapping error train models . . . . .	53
5.5	Landmark Mapping error multi-model configuration. . . . .	54
5.6	Landmark Mapping error single-model configuration. . . . .	54





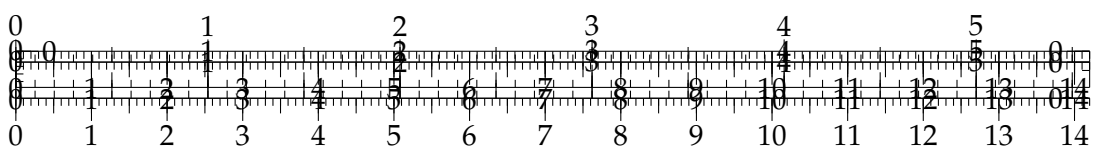
5.7	Landmark Mapping error over the trajectory range in multi-model configuration. . . . .	55
5.8	Landmark Mapping error over the trajectory range in single-model configuration. . . . .	55
5.9	Translation error in multi-model configuration. . . . .	57
5.10	Translation error in single-model configuration. . . . .	57
5.11	Rotation error in single-model configuration. . . . .	58
5.12	Rotation error in single-model configuration. . . . .	58
5.13	2D error over the test dataset. . . . .	62
5.14	Landmark Regression error on test dataset . . . . .	62
5.15	Landmark Mapping error in multi-model configuration on test dataset. . . . .	63
5.16	Landmark Mapping error in single-model configuration on test dataset. . . . .	63
5.17	Landmark Mapping error over the trajectory range in the multi-model configuration on test dataset. . . . .	64
5.18	Landmark Mapping error over the trajectory range in the single-model configuration on test dataset. . . . .	64
5.19	Translation error over the trajectory range in multi-model configuration on test dataset. . . . .	65
5.20	Translation error over the trajectory range in single-model configuration on test dataset. . . . .	65
5.21	Rotation error over the trajectory range in multi-model configuration on test dataset. . . . .	66
5.22	Rotation error over the trajectory range in single-model configuration on test dataset. . . . .	66



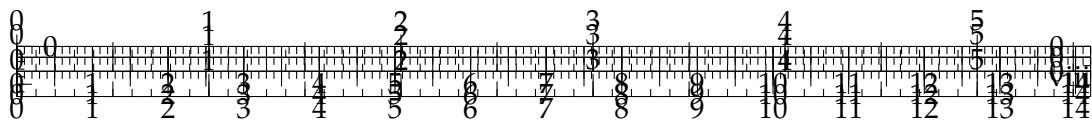


# List of Tables

1.1	Specifics of the simulated training trajectories. . . . .	4
2.1	Physical characteristics of a Flexar coil . . . . .	16
2.2	Magnetic field remanence of different N grade neodymium magnets. .	24
4.1	Specifics of three models $M1$ , $M2$ and $M3$ . . . . .	42
5.1	Landmark Regression module results. . . . .	52
5.2	Thresholds of the multi-model configuration. . . . .	52
5.3	Landmark Mapping module results with single and multi-model configurations. . . . .	56
5.4	Results on training set with multi-model configuration. . . . .	59
5.5	Results on training set with single-model configuration. . . . .	59
5.6	Results on test set with multi-model configuration. . . . .	67
5.7	Results on test set with single-model configuration. . . . .	67

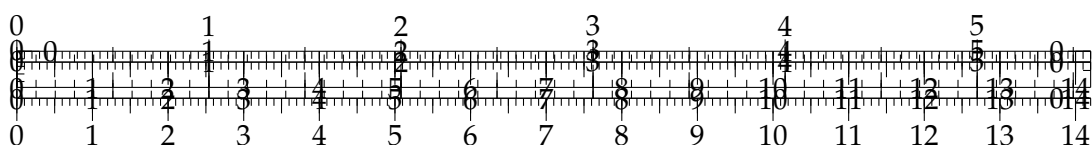


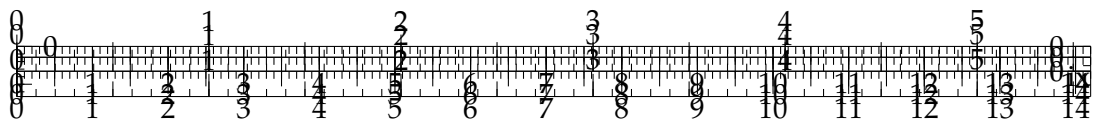




# List of Abbreviations

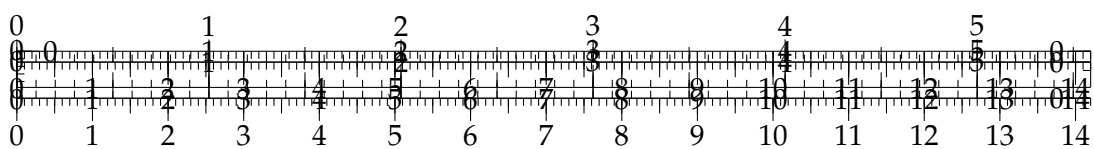
PCB	Printed Circuit Board
AC	Alternated Current
DC	Direct Current
AI	Artificial Intelligence
CAD	Computer-Aided Design
CNN	Convolutional Neural Network
CPD	Coherent Point Drift
CV	Computer Vision
D	Dimension(s)
DOF	Degrees Of Freedom
EM	Expectation- <b>Maximization</b>
EROSS	European Robotic Orbital Support Services
EU	European Union
FAIR	Facebook's AI Research lab
FOV	Field Of View
GEO	Geostationary Equatorial Orbit
GMM	Gaussian Mixture <b>Model</b>
GPU	Graphics Processing Unit
HRNet	<b>High-Resolution Network</b>
ICP	Iterative Closest Point
IOD	In Orbit Demonstration
LEO	Low Earth Orbit
ML	Machine Learning
MSE	Mean Squared Error
NN	Neural Network
RANSAC	<b>Random Sample Consensus</b>
R-CNN	Region-based Convolutional Neural Network
RPY	Roll, Pitch, Yaw
SIFT	Scale Invariant Feature Transform
SURF	Speeded Up Robust Feature
MSER	Maximally Stable Extremal Regions
BRIEF	Binary Robust Independent Elementary Features
PnP	Perspective- <b>n</b> -Point
SfM	Structure from Motion
SPN	Spacecraft Pose Network
SWaP	Size Weight and Power

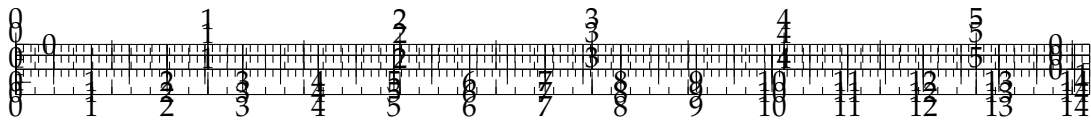




# List of Symbols

Symbol	Name	Unit
$E_{CNN}$	Landmark Regression error	px
$E_{NN}$	Landmark Mapping error	cm
$E_T$	Translation error	cm
$E_R$	Rotation error	°
$S_T$	Translation score	-
$S_R$	Rotation error	rad





## Chapter 1

# Introduction

### 1.1 Thesis objective

In the expanse of space, satellite missions and on-orbit services have become critical assets, serving a myriad of applications including Earth observation, global communication, and scientific research.

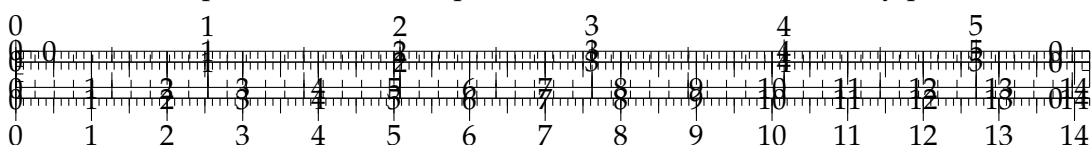
The progressive introduction of AI algorithms into various environments, including space applications, represents a significant leap forward in technological advancement. In the context of pose estimation in space, the incorporation of AI brings a multitude of benefits that enhance the autonomy of satellite operations.

In recent years, we've witnessed a rapid proliferation of on-orbit satellites, driven by advancements in technology and the need for enhanced space services. As the number of these satellites continues to rise, the complexities associated with their safe and effective navigation, rendezvous, and scientific missions have grown in tandem. This is where AI shines, as it steps in to revolutionize the field of satellite pose estimation.

In the 2019 the EU funded EROSS [4], a project, with the goal of showcasing key European solutions for "Servicer" and "Client" vehicles, designed to be used in both low Earth orbit (LEO) and geostationary equatorial orbit (GEO). This initiative aims to enhance the availability of cost-effective and secure orbital services by assessing and validating the essential technological components of the Servicer spacecraft. These components are crucial for executing various tasks during satellite servicing operations, such as rendezvous, capture, grasping, berthing, and manipulation of a non-collaborative Client satellites. As a result, the incorporation of robotic space technologies will lead to greater autonomy and safety in executing these services in space, requiring reduced ground-based supervision.

AI algorithms, equipped with their machine learning capabilities, enable satellites to process vast amounts of data from onboard sensors with remarkable precision and efficiency. This means an elevated level of accuracy in determining a satellite's position, orientation, and trajectory. But the benefits go beyond mere precision.

AI algorithms, equipped with their machine learning capabilities, enable satellites to process vast amounts of data from onboard sensors with remarkable precision and efficiency. One remarkable development is the ability to estimate a satellite's position and orientation using just a single camera, eliminating the need for a stereocamera setup. This innovation not only enhances accuracy but also reduces hardware complexity, making satellite design more cost-effective. AI-driven monocular camera-based pose estimation empowers satellites to autonomously process visual



data, adjust to dynamic orbital environments, and make informed decisions, even in the midst of complex maneuvers, ensuring the mission's success and safety.

Moreover, the increased autonomy provided by AI minimizes the need for constant human intervention and ground control. This not only reduces operational costs but also allows human operators to focus on more strategic aspects of the mission, enhancing productivity and mission efficiency. As we look to the future, AI algorithms promise to usher in a new era of space exploration and satellite operations.

In summary, the progressive introduction of AI algorithms in space applications, particularly in pose estimation, opens the door to enhanced accuracy, real-time adaptability, autonomy, and overall mission efficiency. This transformative technology propels us closer to unlocking the full potential of space exploration and satellite services.

The objective of this thesis is to implement the rendezvous of a collaborative satellite using AI algorithms, with a particular emphasis on their applications in mono camera-based visual pose estimation. The focus is specifically directed towards a detailed analysis of rendezvous operations within the 200-20cm distance range from a non-cooperative satellite. This project delves into the critical aspects of pose estimation throughout the entire trajectory of the rendezvous process, extending from the initial approach to the final berthing phase.

## 1.2 Necessary background (?)

The algorithm is designed around *TASI EROSS IOD Simulated Dataset N°2*, which consists of grayscale images of the satellite; see figure 1.1.

The training dataset is composed of sixteen trajectories each of 900 images. Each trajectory covers the distance range from 200 to 20 cm to the target and the difference between each subsequent frame captured by each camera is 0.2 cm. Each image is of size 512x512 pixels and it's paired with ground truth 6DOF poses (position and orientation).

Figures/Chapter1/DatasetExample.png

FIGURE 1.1: Sample images from the *TASI EROSS IOD Simulated Dataset N°2*

The data acquisition has been performed as follow:

- **Non Prepared scenario:** LAR view.
- **Natural Illumination:** Full illumination (sun @45°, 130k lux).
- **Illumination system:** ON (150lm x6 LEDs).
- **Simulated Camera Settings:**
  - Shutter speed: 20
  - ISO: 5
  - Aperture: 4
  - FOV: 67.8°
- **Reference System:**
  - Left-handed XYZ reference.
  - Origin [0,0,0]:
    - \* XY: zeroes on the vertical symmetry axis of the Target.
    - \* Z: Positive towards contact, zeroed on the lowest contact point of the LAR.
  - All units are in centimeters (cm).
- **Trajectories:**
  - all trajectories follow the same XYZ coordinates.
  - the rotation is considered with Euler angles as Pitch (around axis x), Yaw (around axis y) and Roll (around axis z), all positive counterclockwise. Trajectories' specifics are reported in table 1.1.
  - Camera pointing XY in [-46, +20].

Figures/Chapter1/UPS.png

FIGURE 1.2: Model's UPS

TABLE 1.1: Specifics of the simulated training trajectories.

Trajectory	Roll(°)	Pitch(°)	Yaw(°)
TRAY_1	0	0	0
TRAY_2	0	0	-1
TRAY_3	0	0	-2
TRAY_4	0	0	-3
TRAY_5	0	0	-4
TRAY_6	0	0	-5
TRAY_7	0	1	0
TRAY_8	0	2	0
TRAY_9	0	3	0
TRAY_10	0	4	0
TRAY_11	0	5	0
TRAY_12	-1	0	0
TRAY_13	-2	0	0
TRAY_14	-3	0	0
TRAY_15	-4	0	0
TRAY_16	-5	0	0

The *TASI EROSS IOD Simulated Dataset N°3* along with the *Less\_Difficult\_Trajectory* and *Difficult\_Trajectory* are used as the test dataset. The *TASI EROSS N°3* is composed of two trajectories, each of which was captured with two different camera positions. Each trajectory has 900 images.

The *TRAY\_A* starts with  $+15^\circ$  on Yaw and linearly converge toward 0 on contact, while *TRAY\_B*, *Less\_Difficult\_Trajectory* and *Difficult\_Trajectory* present multiple errors on RPY converging toward 0 on contact as well.

### 1.3 Thesis structure

The thesis is structured in further five chapters:

#### Chapter 2 - Background:

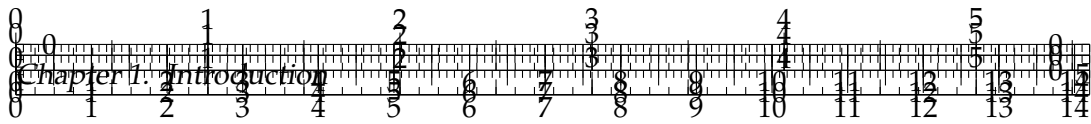
This chapter provides a comprehensive overview of key concepts necessary for the correct understanding of this work, with a focus on monocular camera models, perspective projection, pose estimation, and a general introduction to deep learning models.

#### Chapter 3 - State-of-art:

This chapter delves into monocular pose estimation methods, covering classic approaches like RANSAC and SfM, and exploring modern techniques such as end-to-end learning with networks like PoseNet and Mask R-CNN. The chapter also introduces feature learning, emphasizing CNN-based methods like HRNet for predicting 2D landmark locations. Moreover, some studies about spacecraft pose estimation and their use of deep learning architectures are presented. The chapter also delves into point set alignments, highlighting the widely used and advanced algorithms like Coherent Point Drift (CPD) technique employed in the method for final pose estimation.

#### Chapter 4 - Algorithms and Methods:

This chapter delves into the methodology's core algorithms and techniques. It



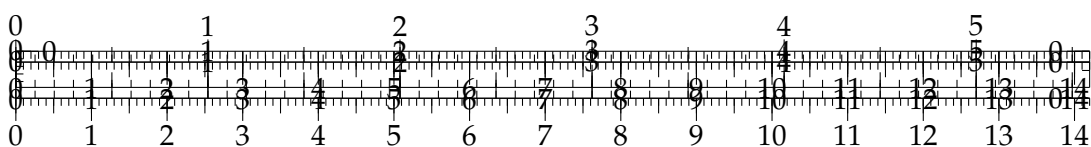
outlines the offline architecture, detailing the 2D-3D correspondence process, landmark regression, and the neural network-based landmark mapping. The chapter then presents the online architecture, covering real-time processing and the Coherent Point Drift technique for pose estimation. Implementation challenges and dataset considerations are also discussed, providing a comprehensive overview of the applied methods.

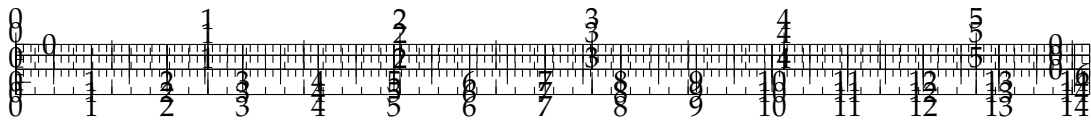
#### **Chapter 5 - Implementation and Experiments:**

This chapter presents the tools and technologies employed for the project implementation and the evaluation metrics for pose estimation, Landmark Regression, Landmark Mapping are described. The chapter culminates in the assessment of both training and test datasets, showcasing the method's robustness and generalization across diverse scenarios. Overall, it provides comprehensive exploration of the research's implementation and experimentation phases.

#### **Chapter 6 - Discussions and Conclusions:**

The Chapter delves into challenges faced by on-board AI systems in space missions, focusing on verifiability and computational load. It emphasizes the significance of minimizing translation errors for accurate maneuvering in the proposed multi-model configuration. The section explores potential improvements, including enhanced landmark selection and strategies to fortify system robustness.





## Chapter 2

# Background

### 2.1 Magnetic Coils

#### 2.1.1 Brief History

The connection between electricity and magnetism was first demonstrated by Hans Christian Oersted in 1820 when he observed that an electric current flowing through a wire could deflect a nearby magnetic needle.

Meanwhile, the creation of the first practical electromagnet is credited to William Sturgeon and André-Marie Ampère who after Oersted's discovery experimented with creating coil windings wrapped around an iron core which allowed them to achieve much stronger magnetic fields.

During the 1830's Michael Faraday's discovery of electromagnetic induction further advanced the understanding of magnetic fields and coils. Faraday demonstrated that a changing magnetic field could induce an electric current in a nearby conductor, laying the groundwork for transformers and modern electrical generators.

The latter half of the 19th century saw rapid advancements in electrical engineering. Innovations like early electric generators (dynamoes), transformers, and electric motors heavily relied on magnetic coils for their operation. Researchers such as Nikola Tesla and Thomas Edison further developed these technologies.

Magnetic coils continue to play a vital role in various fields, including power generation, telecommunications, electronics, and medical imaging (such as MRI machines). With advancements in materials science and manufacturing techniques, magnetic coils have become more efficient, compact, and versatile.

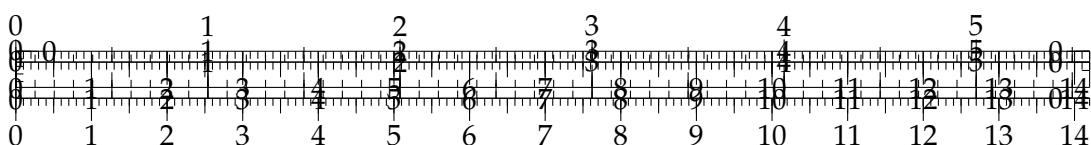
In recent years, as the use of PCBs has become widespread, researchers started experimenting with creating coil windings utilizing this technology.

#### 2.1.2 Physics of an inductor?

##### Inductance

All conductors have some inductance, which may have either desirable or detrimental effects in practical electrical devices. The inductance of a circuit depends on the geometry of the current path and the magnetic permeability of nearby materials.

Any alteration to a circuit that increases the flux (total magnetic field) through the circuit produced by a given current increases the inductance, because inductance is equal to the ratio of magnetic flux to current





$$L = \frac{\Phi(i)}{i} \quad (2.1)$$

Where:

- $L$  is the inductance [H].
- $i$  is the current [A].
- $\Phi(i)$  is the magnetic flux through the circuit [Wb].

### Reactance

When a current signal is applied to an inductor, a flux is generated and, considering Faraday's law of induction, any change in flux through a circuit induces an electromotive force  $\mathcal{E}$ , proportional to the rate of change of flux

$$\mathcal{E} = -L \frac{d\Phi(t)}{dt} \quad (2.2)$$

Then using Lenz's law, the voltage across the inductor is given by

$$V = -L \frac{di}{dt} \quad (2.3)$$

Inductors resist changes in current due to the magnetic field they generate when current passes through them. When we apply a sinusoidal signal to our inductor, the current will be continuously changing direction. The inductor's opposition to these changes is represented as reactance.

Inductive reactance ( $X_L$ ) is measured in ohms and is calculated using the formula:

$$X_L = 2\pi fL \quad (2.4)$$

Where:

- $X_L$  = Inductive reactance [ $\Omega$ ]
- $f$  = Frequency of the AC current [Hz]
- $L$  = Inductance of the inductor [H]

We can then calculate the total impedance of the inductor as

$$Z = \sqrt{R^2 + X_L^2} \quad (2.5)$$

Where:

- $Z$  = Total impedance [ $\Omega$ ]
- $R$  = Resistance of the inductor [ $\Omega$ ]
- $X_L$  = Inductive reactance [ $\Omega$ ]

## Joule heating

Inductors are passive components, meaning they do not generate energy. However, they do store energy in the form of a magnetic field. When the current through an inductor changes, the magnetic field changes, and energy is stored in the field. When the current decreases, the magnetic field collapses, and the energy is returned to the circuit. This energy is dissipated as heat in the inductor's windings.

The power dissipated in an inductor is given by the relation

$$P = |I_{RMS}|^2 R = \frac{|V_{RMS}|^2}{|Z|^2} R \quad (2.6)$$

Where:

- $P$  = Power dissipated in the inductor [W]
- $I$  = Current flowing through the inductor [A]
- $R$  = Resistance of the inductor [ $\Omega$ ]
- $V$  = Voltage across the inductor [V]
- $Z$  = Total impedance of the inductor [ $\Omega$ ]

## Definition of Root Mean Square (RMS) values

As we have seen in the previous paragraphs, the power dissipated by the coil depends on the root mean square values of the current and voltage. We use the RMS values because they allow us to compare the power dissipated by the coil when powered in AC and DC conditions. For DC signals these values are equal to the DC one, while for sinusoidal signals  $V_{RMS}$  can be calculated as

$$V_{RMS} = \sqrt{\frac{1}{T} \int_0^T [f(t)]^2 dt} \quad (2.7)$$

Where:

- $T$  is the period of the input signal
- $f(t)$  is the function of the signal

Then in case we're dealing with AC signals having a DC offset we can use the formula

$$V_{RMS_{AC+DC}} = \sqrt{V_{DC}^2 + V_{RMS_{AC}}^2} \quad (2.8)$$

Some formulas for important waveforms:

### 2.1.3 Magnetic field generation

The strength of the magnetic field on the z-axis of the coil is derived from the Biot-Savart Law and is given by the formula

Name	Waveform	$V_{RMS}$
DC	$V_P$	$V_P$
Sine Wave $[-V_P, V_P]$	$V_P \sin(2\pi ft)$	$\frac{V_P}{\sqrt{2}}$
Polarized Sine Wave $[0, V_P]$	$\frac{V_P}{2} (\sin(2\pi ft) + 1)$	$\frac{V_P}{2} \sqrt{\frac{3}{2}}$
Square Wave $[-V_P, V_P]$	$V_P \text{sgn}(\sin(2\pi ft))$	$V_P$
DC-shifted Square Wave $V_{DC} + [-V_P, V_P]$	$V_{DC} + V_P \text{sgn}(\sin(2\pi ft))$	$\sqrt{V_{DC}^2 + V_P^2}$

FIGURE 2.1: RMS values for different waveforms.



$$B_z = \frac{N\mu I r^2}{2(r^2 + z^2)^{\frac{3}{2}}} \quad (2.9)$$

Where:

- $B_z$  is the magnetic field on the z-axis [T].
- $\mu$  is the magnetic permeability of the medium [H/m].
- $I$  is the current flowing through the wire [A].
- $r$  is the radius of the coil [m].
- $N$  is the number of turns of wire in the coil.
- $z$  is the z-distance from the center of the coil [m].

If the coil lacks a core the permeability of free space is used instead of the core's permeability; instead if wound on a ferromagnetic core the permeability of the core is calculated as

$$\mu = \mu_0 \cdot \mu_r$$

where  $\mu_r$  is the relative permeability of the core material.

With the right material for the core, the magnetic field intensity can be highly increased compared to the field generated by the coil alone.

IL FOTTUTO GRAFICO A BARRE DELLA PERMEABILITA'

### Magnetic Flux and Field relation

We can also relate the magnetic field to the magnetic flux generated by the coil. The magnetic flux is given by the formula

$$\Phi_B = B \cdot A \quad (2.10)$$

Where:

- $\Phi_B$  is the magnetic flux [Wb].
- $B$  is the magnetic field [T].
- $A$  is the area of the coil [m<sup>2</sup>].

## 2.2 PCB Coils

The biggest problem with standard coils is their size, especially in the z-direction as the more windings are used the thicker they will become. This is a problem for applications where space is limited, such as in the case of implantable devices. To address this issue, researchers have started to experiment with creating coil windings using PCB technology. This allows for the creation of coils that are thinner and more compact than traditional coils. In this section, we will discuss the different types of PCB coils and the challenges associated with their miniaturization.

### 2.2.1 Planar coils

As PCBs are 2D objects we can't work on the z-axis to create the coil's windings. This means that the windings have to be created on the same plane. In 1984 researchers from Osaka University proposed the first implementation of a possible solution in the form of planar coils. They proposed and tested a structure comprised of concentric spirals, with different shapes, made of a conductive material (mostly copper) suspended in an insulation material and then covered by two magnetic material layers (???) [10].

./svg-inkscape/planar\_coil\_svg-tex.pdf

With the mainstream adoption of PCBs in the electronics industry, researchers have created planar coils using PCBs by etching spiral patterns on the copper layer. This allowed for the production of planar coils easily and cheaply.

The main advantage of planar coils is that they can be easily integrated into the PCB design, reducing the overall size of the device. This is particularly useful in the case of wireless power transfer systems, where the coils are used to transfer power between devices. The smaller size of the coils allows for more compact and portable devices.

Another advantage is the ability to design coils of arbitrary shapes and sizes, depending on the requirements of the application. This flexibility allows for the creation of coils that are optimized for specific applications and PCB shapes, resulting in improved performance.

Chapters/Chapter2/PCB\_coils/Figures/coils\_shapes.png

FIGURE 2.2: Different planar coil architectures such as (a) triangle, (b) square, (c) pentagon, (d) hexagon, (e) circle.

## 2.2.2 Planar coil magnetic field

The structure of a planar coil is very different from a standard one, as it is a flat structure with a spiral winding. The magnetic field generated by a planar coil is more complex than that of a standard coil, as the magnetic field is not concentrated in the center of the coil but is distributed over the entire surface of the coil. The magnetic field generated by a planar coil is represented in Figure 2.3

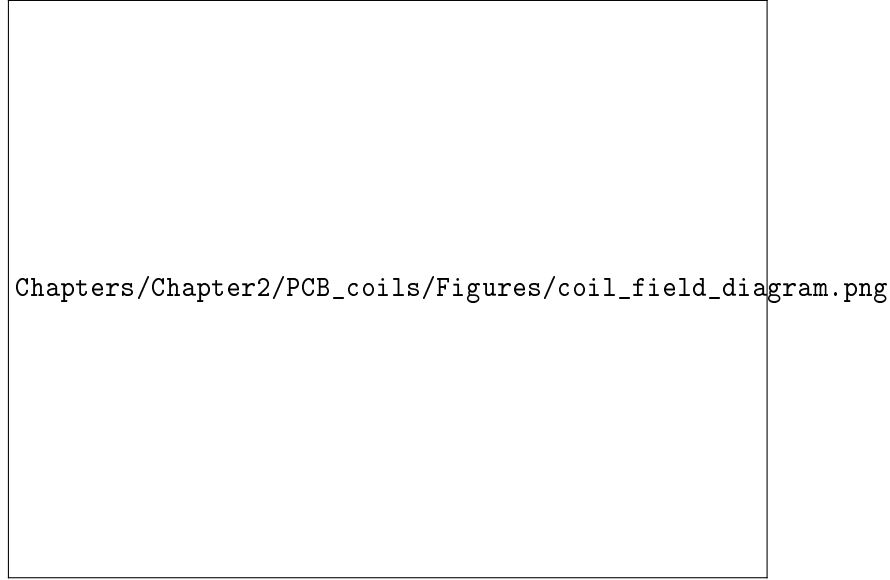


FIGURE 2.3: (c) Representation of the magnetic field generated by a circular spiral planar coil placed on an aluminum plate.[7]

Then considering again the circular spiral structure, the magnetic field generated by a planar coil at its surface can be derived as

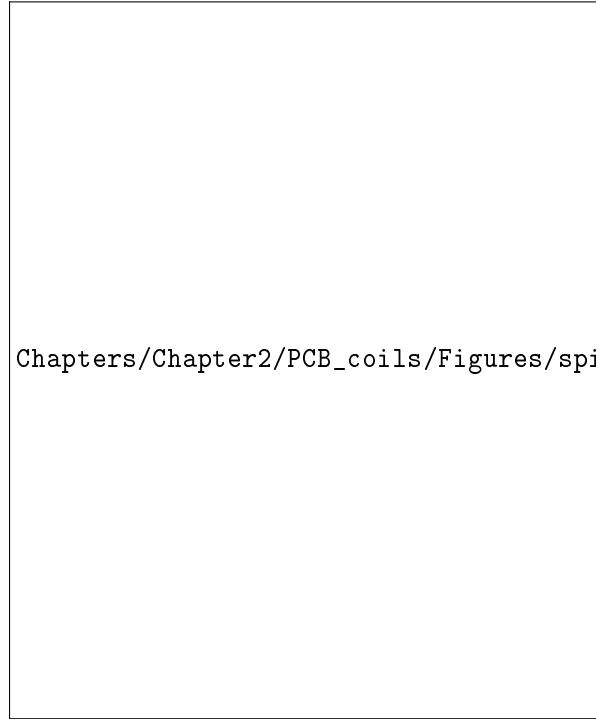
$$B_z = \frac{\mu NI}{2} \cdot \frac{\ln(\frac{b}{a})}{b-a} \quad (2.11)$$

Where:

- $B_z$  is the magnetic field on the z-axis [T]
- $\mu$  is the magnetic permeability of the medium [H/m]
- $n$  is the number of turns of the spiral
- $I$  is the current flowing through the wire [A]
- $b$  is the external radius of the spiral [m]
- $a$  is the internal radius of the spiral [m]

To then find the magnetic field at a distance  $z$  from the center of the coil, we can use the equation (2.9) from the previous subsection and substitute the radius  $r$  of the coil with  $r' = \frac{b-a}{\ln(\frac{b}{a})}$

$$B_z = \frac{\mu NI r'^2}{2(r'^2 + z^2)^{\frac{3}{2}}} \quad (2.12)$$



Chapters/Chapter2/PCB\_coils/Figures/spiral\_windings.jpg

FIGURE 2.4: Circular spiral coil.

### 2.2.3 Multi-layer PCB coils

Another approach to miniaturizing PCB coils is to create multi-layer coils. This is done by stacking multiple layers of PCBs on top of each other, with each layer containing a different part of the coil. This allows for the creation of coils with a higher number of windings in a smaller space. The main challenge with multi-layer PCB coils is the alignment of the different layers. If the layers are not aligned properly, the coil will not function correctly.

Current manufacturing allows for up to 10 layers of PCBs to be stacked on top of each other. However, the more layers that are added, the more difficult it becomes to align the layers correctly. If the layers are not aligned properly, the magnetic field generated by each layer will also not be aligned, which can lead to a decrease in the efficiency of the coil due to interferences.

#### Total inductance

Considering a two layers coil the total inductance can be calculated as

$$L_s = 2L_0 + 2M, M = K_c \cdot L_0 \quad (2.13)$$

Where:

- $L_s$  is the total inductance of the coil [H].
- $L_0$  is the inductance of a single layer [H].
- $M$  is the mutual inductance between the two layers [H].
- $K_c$  is the coupling coefficient between the two layers.

Then  $K_c$  can be calculated with an empirical formula derived from multiple measurements by Jonsenser Zhao [37] as

$$K_c = \frac{N^2}{0.64[(0.184d^3 - 0.525d^2 + 1.038d + 1.001)(1.67N^2 - 5.84N + 65)]} \quad (2.14)$$

Where:

- $N$  is the number of turns of the coil.
- $d$  is the distance between the two layers [m].

### Magnetic field generated by a Multilayer coil

We can use equation (2.1) and  $L_s$  calculated in the previous point to find the magnetic flux through the coils

$$\Phi(I) = L_s \cdot I \quad (2.15)$$

Then with equation (2.10) we can derive the total magnetic field as

$$B_t = \frac{L_s \cdot I}{\pi r^2} \quad (2.16)$$

Where:

- $B_t$  is the total magnetic field [T].
- $r$  is the radius of the coil [m].

## 2.3 Flexible PCB coils

Flexible PCB coils are a type of PCB coil that is made using a flexible substrate. This allows for the creation of coils that can be bent and twisted without breaking.

### 2.3.1 Pros of flexible coils

Flexible PCBs (Printed Circuit Boards) offer several advantages over traditional rigid PCBs. Here are some of the key pros of flexible PCBs:

1. **Flexibility and Space Savings:** Flexible PCBs can bend and twist, allowing for compact and efficient use of space in electronic devices.
2. **Lightweight:** The materials used in flexible PCBs are lightweight, making them ideal for applications where weight is a concern, such as in aerospace or portable electronics.
3. **Improved Design Freedom:** Flex PCBs allow for more creative and versatile designs because they can be formed into complex shapes and fit into tight or irregular spaces.
4. **Reduced Connectors and Interconnects:** Because flexible PCBs can bend, they can often eliminate the need for additional connectors and interconnects, reducing overall system complexity.



5. **Vibration and Shock Resistance:** Flexible PCBs can absorb shock and vibrations better than rigid PCBs, making them suitable for use in environments where these are concerns.
6. **Simplified Assembly:** With fewer connectors and interconnects, assembly becomes easier and faster, reducing labor and potential points of failure.
7. **High-Density Interconnects:** Flexible PCBs can support fine-pitch components and high-density interconnects, making them suitable for advanced electronics.

### 2.3.2 Application challenges

As said before flexible PCBs offer great design flexibility and the possibility of implementing innovative designs and devices but they also come with their own set of challenges; especially in the case of flexible coils.

#### Rise of high resistance

Taking as an example the flexible coil we'll be using in our project, the resistance of the coil is  $30\Omega$ . This is a relatively high resistance for a coil, especially when compared to traditional copper wire coils. This is due to the intrinsic structure of PCBs, especially flexible ones. PCBs are created by etching very thin copper traces on a substrate, in the case of flexible PCBs, as the substrate must be flexible, their thickness is even lower and consequently also the traces are.

The coil can be considered as a very long strand of a very thin copper so its resistance can be calculated using the Ohm Law

$$R = \rho \cdot \frac{L}{A} \quad (2.17)$$

Where:

- $R$  is the resistance [ $\Omega$ ].
- $\rho$  is the resistivity of the material [ $\Omega \cdot m$ ].
- $L$  is the length of the conductor [m].
- $A$  is the cross-sectional area of the conductor [ $m^2$ ].

Then to find the length of the copper traces we can use the approximated formula [35]

$$L = N\pi \frac{D + d}{2} \quad (2.18)$$

Where:

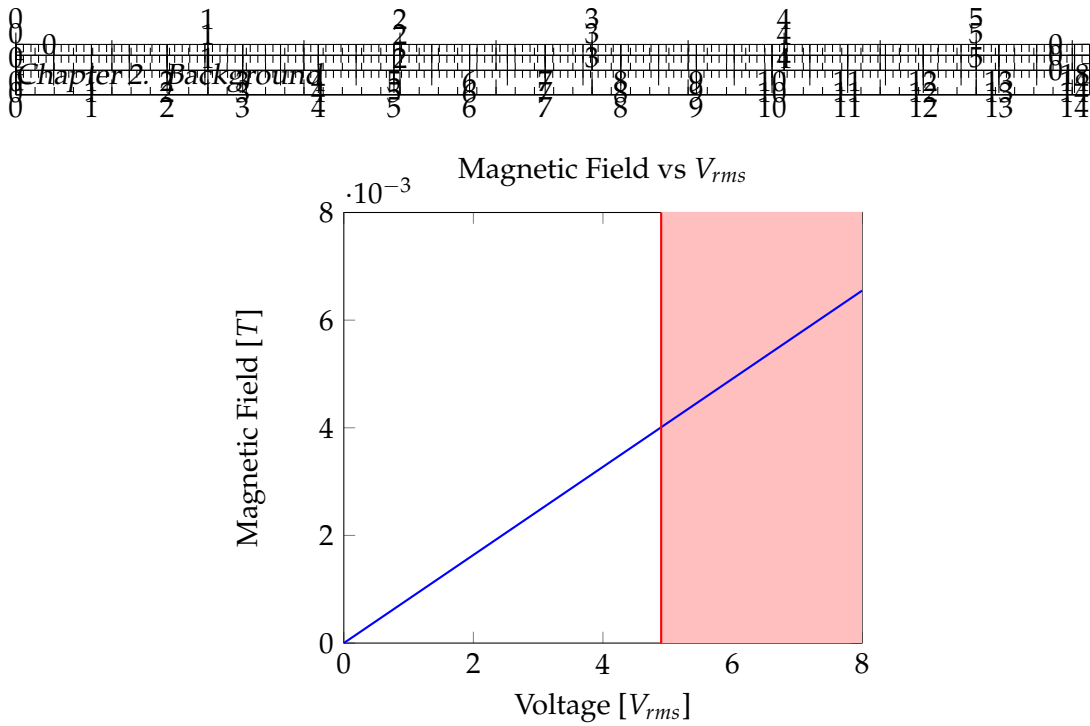
- $N$  is the number of turns.
- $D$  is the outer diameter of the coil [m].
- $d$  is the inner diameter of the coil [m].

The tracks' cross-section is a rectangle so the area can be calculated as

$$A = w \cdot t \quad (2.19)$$

- $P$  is the power dissipated by the coil [W].





As we can observe even at the power limit of 0.8W (  $\simeq 5V$  ) the magnetic field generated by the coil is very low (  $\simeq 4mT$  ).

### Resistance parasitic effects due to AC current

This paragraph will be a brief introduction to the parasitic effects that can occur in a coil due to the AC current that flows through it. All these effects are negligible at low frequencies (up to about 1kHz) which is the range we are aiming for in this project, but we will explore them for the sake of future research.

The main parasitic effects that can occur in a coil are:

- **Reactance:** This is the opposition that a coil offers to the flow of AC current. This is due to the self-inductance of the coil which opposes the change in current flowing through it. This effect can lead to a change in the effective resistance of the coil.

The reactance of a coil can be calculated using the formula

$$X_L = 2\pi fL \quad (2.22)$$

Where:

- $X_L$  is the reactance of the coil [ $\Omega$ ].
- $f$  is the frequency of the AC current [Hz].
- $L$  is the inductance of the coil [H].

Then the impedance of the coil can be calculated as

$$Z = \sqrt{R_{DC}^2 + X_L^2} \quad (2.23)$$

- **Skin effect:** This effect is due to the current flowing through a conductor tending to flow on the surface of the conductor. This gives rise to a thin layer inside the conductor where all the current flows. As a result, the effective resistance of the conductor increases. This effect is more pronounced at higher frequencies.

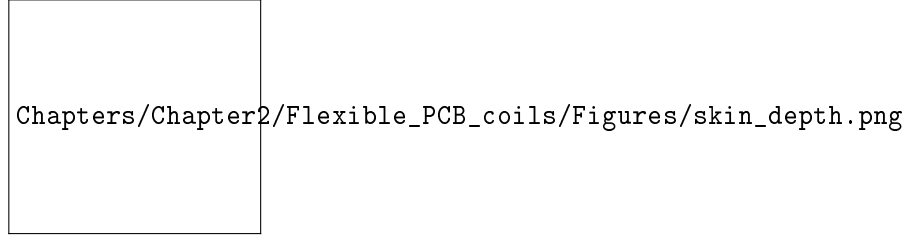


FIGURE 2.5: (c) Representation of the thin surface generated by the skin effect

The thickness of this area is called the **skin depth** and can be calculated using the formula

$$\delta = \sqrt{\frac{\rho}{\mu\pi f}} \quad (2.24)$$

Where:

- $\delta$  is the skin depth [m].
- $\rho$  is the resistivity of the conductor [ $\Omega \cdot m$ ].
- $\mu$  is the magnetic permeability of the medium [H/m].

The effective resistance of the conductor can be derived from the skin depth using Dowell's equation

$$R_{skin} = F_{skin} \cdot R_{DC} \quad (2.25)$$

and

$$F_{skin} = \frac{1}{2} \left( \frac{h}{\delta} \right) \frac{\sinh(\frac{h}{\delta}) + \sin(\frac{h}{\delta})}{\cosh(\frac{h}{\delta}) - \cos(\frac{h}{\delta})} \quad (2.26)$$

Where:

- $R_{skin}$  is the effective resistance of the conductor due to the skin effect [ $\Omega$ ].
- $F_{skin}$  is the skin effect factor.
- $h$  is the thickness of the conductor [m].

In the case of the coil we're studying, the skin effect is negligible up to 1e8Hz as the thickness of the flexible PCB's traces is very low.

But we can observe from the study done on thicker traces' (0.5mm) coils that the skin effect starts to be already noticeable at 1e5Hz.

- **Proximity effect:** This effect is similar to the skin effect but it occurs when two conductors are close to each other. The current flowing through one conductor induces an eddy current in the other conductor which can lead to a change in the effective resistance of the conductors.

The contribution of the proximity effect to the effective resistance of the coil can be calculated using the formula (considering current flowing in the coil  $I_{ex} = 1A$ ) [21]

$$R_{proximity} = \frac{1}{12} h \sigma \pi^2 f^2 B_n^2 w^3 \quad (2.27)$$

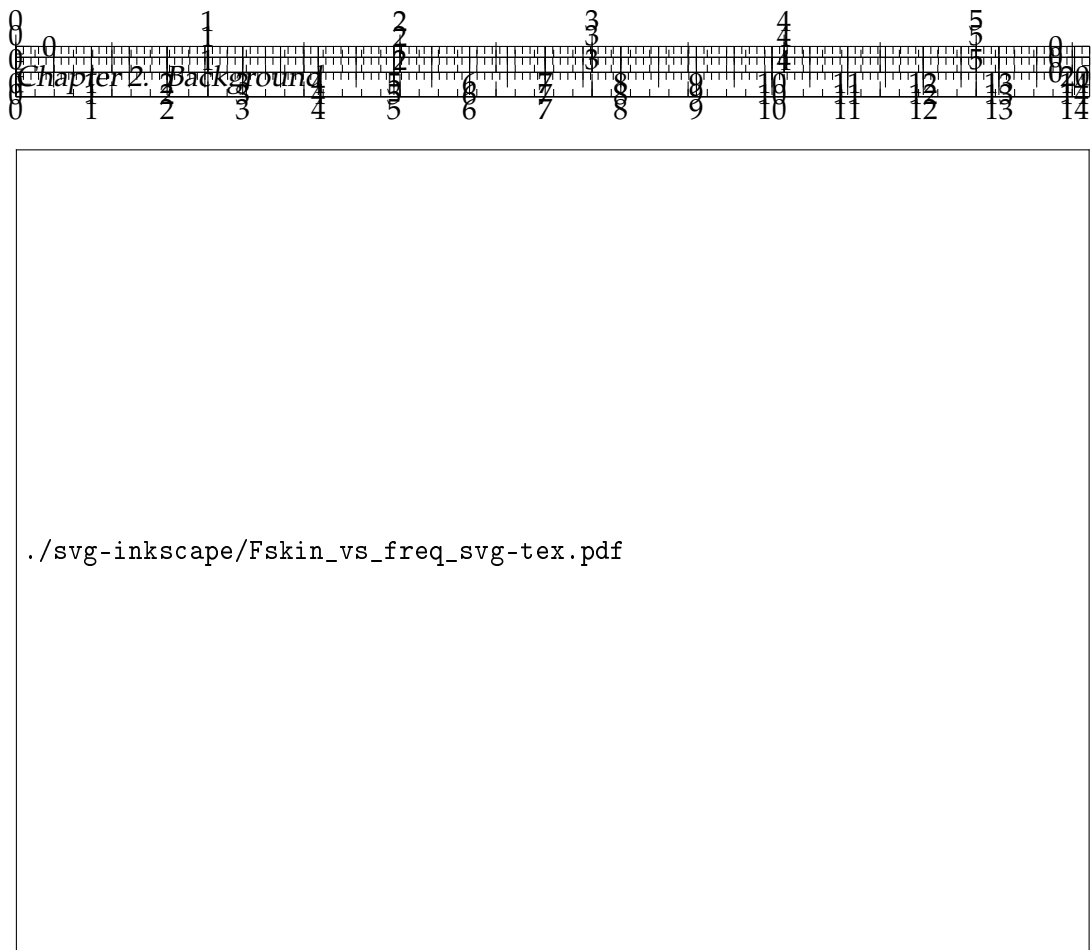


FIGURE 2.6: Logarithmic plot of the skin effect factor for a flexible PCB coil

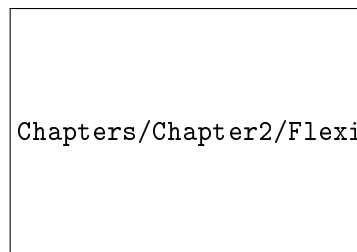


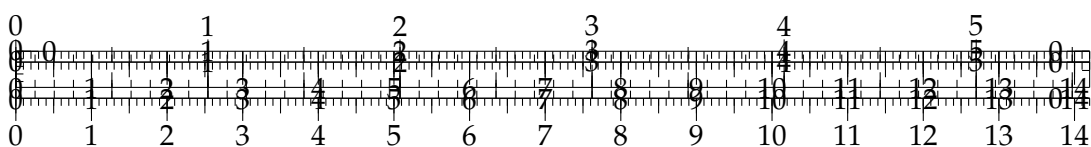
FIGURE 2.7: Skin effect on thicker traces [22]

Where:

- $\sigma$  is the conductivity of the conductor [ $\Omega^{-1} \cdot m^{-1}$ ].
- $h$  is the thickness of the conductor [m].
- $f$  is the frequency of the AC current [Hz].
- $B_n$  is the average external magnetic field [T].
- $w$  is the width of the conductor [m].

We can also approximate  $F_{proximity}$  ( $F_{proximity} = R_{proximity} / R_{DC}$ ) as

$$F_{proximity} = \frac{F_{skin}}{3} \quad (2.28)$$



So when the contribution of the skin effect is negligible, the proximity effect will be negligible as well.

## High current needs

$$I = \sqrt{\frac{P_{max}}{R}} = \sqrt{\frac{0.8}{30}} = 0.1633A \quad (2.29)$$

The solution is to use a special type of Op Amps called power Op Amps, these devices are designed to provide high current outputs. They are usually designed as simple op-amps with a power stage at the output.

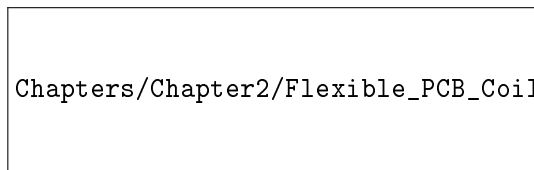


FIGURE 2.9: Power Op Amp block diagram.

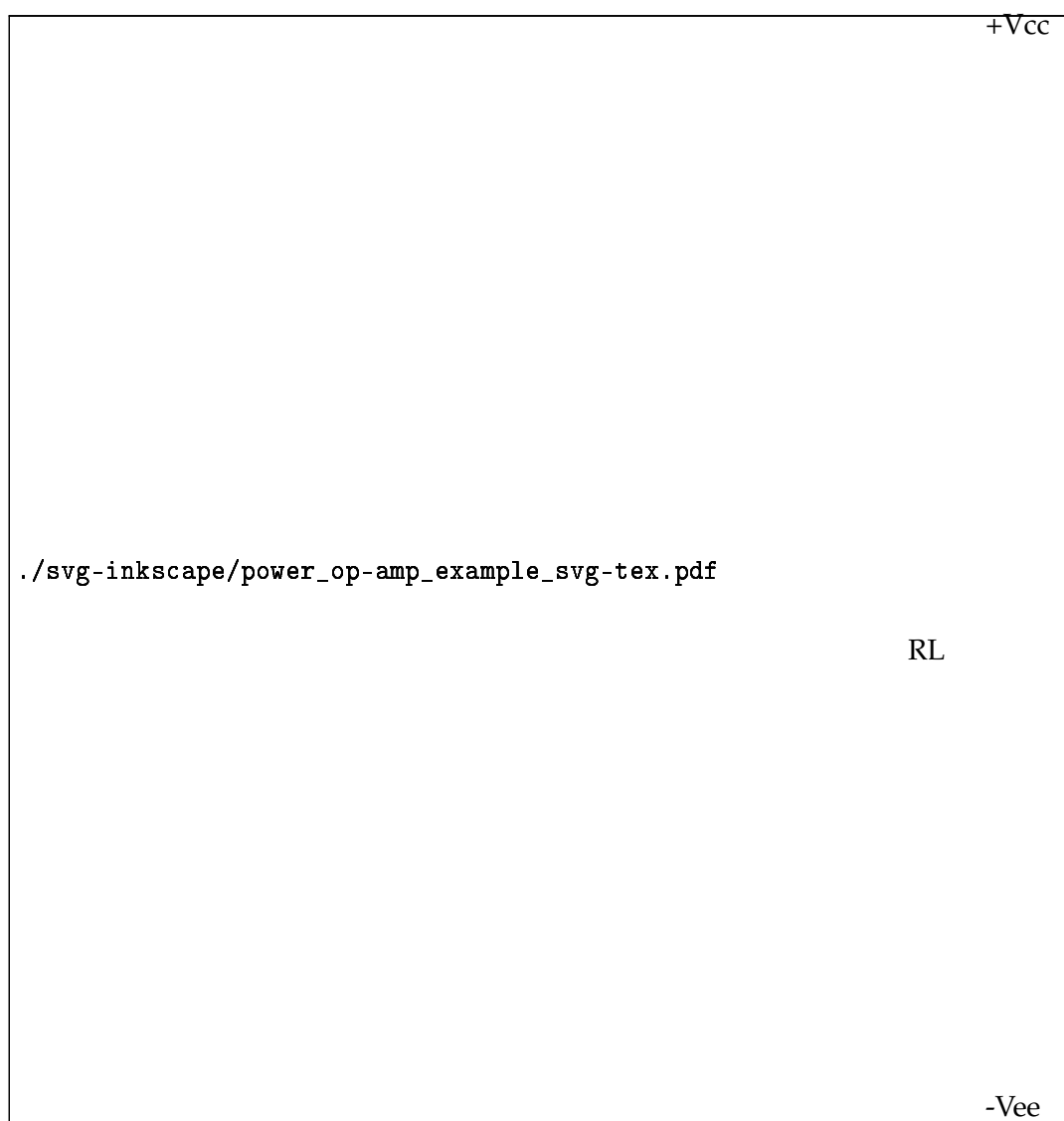


FIGURE 2.10: Example schematic of a power op-amp with a Class-AB power stage.



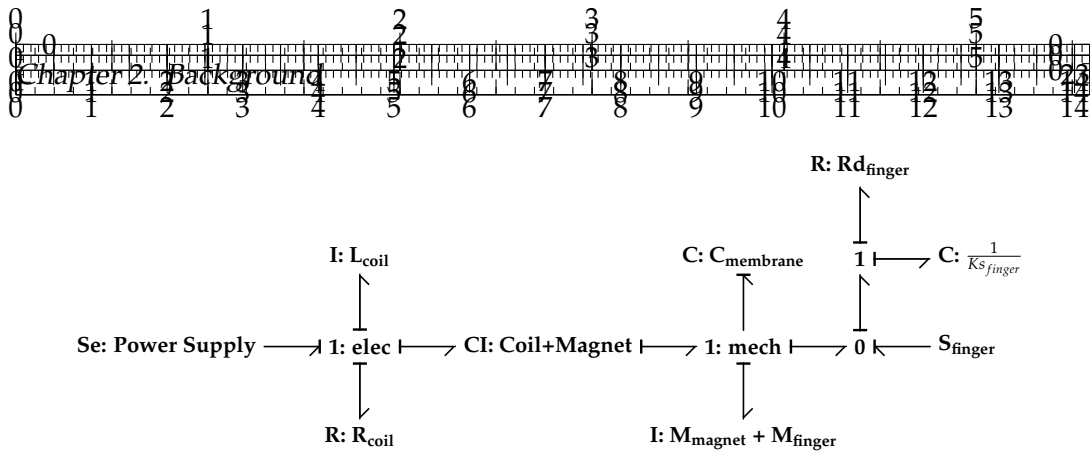


FIGURE 2.11: Bond graph of the coil-magnet-membrane system.

### Constant Voltage vs Constant Current power supplying

To power our coil we have two options, we can either provide a constant voltage or a constant current. Using a constant current source is not advisable due to the heating problem of the coil, at high currents as the coil is run it will heat up and its resistance will increase which will cause the power source to increase the voltage to keep the current constant. This in turn will cause the coil to heat up even more and the cycle will continue until the coil is damaged.

Instead, using a constant voltage source as the resistance increases due to the coil exceeding the heating and power threshold we will only have a decrease in the current which results in a loss of magnetic field strength but the coil won't get damaged.

## 2.4 Modelling of the Entire System

To be able to produce vibrations using the magnetic field produced by the coil we need to introduce to the system an object that can react to the magnetic field. As the magnetic field of the coil is very feeble we can use as the object Neodymium magnets, these are permanent magnets with a very strong internal magnetic field for their size. Using small ones and with the right pole facing the coil (same polarity as the generated magnetic field) it will be able to repel them and make them vibrate. Then to constrain the motion of the magnet and make it only move in the z-axis we have to add to the system a flexible membrane.

We can now model the entire system using a bond graph, as shown in figure 2.11.

In the next subsections, we will analyze the physical laws that govern the behavior of the system and how to model them to create this bond graph.

### 2.4.1 Neodymium magnets (magnetic strength wrt class and dimensions)

Neodymium magnets are a type of rare-earth magnet, they are the strongest type of permanent magnets made commercially. They are made of an alloy of neodymium, iron, and boron and their strength depends on the percentage of neodymium in the alloy and on its crystalline structure. They are classified based on their maximum energy product, which is the maximum amount of energy that can be stored in a magnet. Modern neodymium magnets start from N35 and go up to N52 (even N55), the higher the number the stronger their magnetic field.

Considering a cylindrical magnet with a radius  $R_M$  and a thickness  $t$  we can calculate the magnetic field generated by it at a distance  $z$  from a pole surface using the

Goudsmit Grade	Remanence $B_r$ [mT]	
	min value	typical value
N35	1170	1210
N38	1220	1260
N40	1260	1290
N42	1290	1320
N45	1320	1370
N48	1370	1420
N50	1400	1460
N52	1420	1470

TABLE 2.2: Magnetic field remanence of different N grade neodymium magnets.

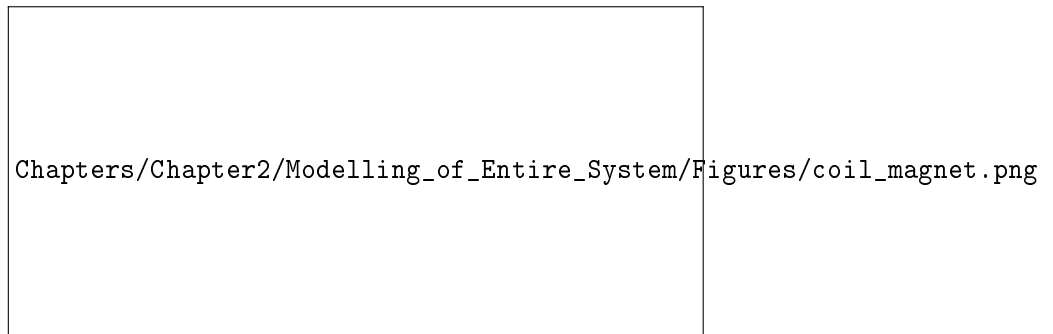


FIGURE 2.12: Coil and magnet position in space.

formula [33]:

$$B_M(z) = \frac{B_r}{2} \left( \frac{t+z}{\sqrt{R_M^2 + (z+t)^2}} - \frac{z}{\sqrt{R_M^2 + z^2}} \right) \quad (2.30)$$

Where:

- $B_r$  is the remanence of the magnet [T]
- $R_M$  is the radius of the magnet [m]
- $t$  is the thickness of the magnet [m]
- $z$  is the distance from a pole surface of the magnet [m]

The remanence of a magnet is the magnetic field that remains in the magnet after the external magnetic field is removed and depends on the N grade of the magnet.

## 2.4.2 Magnetic force between magnet and coil

To calculate the magnetic repulsion force between the coil and a permanent magnet we consider them aligned with their centers coinciding on the z-axis.

The force between a magnet and a coil can be calculated using the magnetic field generated by the coil and magnet. Knowing their closed-form expression we can calculate the force using this formula:

$$F = \nabla(\vec{m}_M \cdot \vec{B}_C) \quad (2.31)$$

Where:

- $\vec{m}_M$  is the magnetic moment of the magnet [A/m]
- $\vec{B}_C$  is the magnetic field generated by the coil [T]

The magnetic momentum of the magnet is defined as:

$$\vec{m}_M = \begin{pmatrix} 0 & 0 & \frac{B_M(z)}{\mu} \end{pmatrix} \quad (2.32)$$

Where:

- $B_M(z)$  is the magnetic field generated by the permanent magnet [T]
- $\mu$  is the magnetic permeability of the medium [H/m]

We can calculate the magnetic field generated by the coil at a distance using equation (2.12) (considering our coil as two in parallel) and the magnetic field generated by a cylindrical magnet at a distance  $z$  using equation (2.30).

Doing the calculations, the resulting force in function of the distance  $z$  is given by:

$$F = \frac{B_r I N R_C^2 \left( \frac{1}{\sqrt{\sigma_1}} - \frac{1}{\sqrt{\sigma_2}} + \frac{z^2}{\sigma_2^{3/2}} - \frac{2(t+z)^2}{2\sigma_1^{3/2}} \right)}{2\sigma_3^{3/2}} + B_C(I) \cdot \frac{3z \left( \frac{z}{\sqrt{\sigma_2}} - \frac{t+z}{\sqrt{\sigma_1}} \right)}{2\sigma_3} \quad (2.33)$$

Where:

- $N$  is the number of spires of a one-layer coil
- $I$  is the current flowing through the coil [A]
- $B_C$  is the coil magnetic field calculated as in (2.12) [T]
- $R_C$  is the coil average radius ( $r'$  in equation (2.12)) [m]
- $\sigma_1 = R_M^2 + (t+z)^2$
- $\sigma_2 = R_M^2 + z^2$
- $\sigma_3 = R_C^2 + z^2$

So we can model the coil-magnet system as a **Transducer** element that converts the current flowing through the coil into a force acting on the magnet.

$$B_C(z, I) = \frac{\mu N I R_C^2}{2(R_C^2 + z^2)^{3/2}} \rightarrow B_C(q, i) = \frac{1}{2} L(q) i \quad (2.34)$$

### 2.4.3 Membrane-magnet system

The magnet needs to be suspended to allow it to move freely only on the  $z$ -axis, to achieve this we need a structure that constrains the lateral motion of the magnet and needs to also be able to vibrate freely with it. To do this we can use a flexible membrane that can deform under the magnetic field generated by the coil and the magnet.

As an example, we will analyze the membrane structure of the last type of prototype we implemented 5.3



FIGURE 2.13: Coil-Magnet Transducer bond graph.

$$F(q, i) = \frac{1}{2} \frac{d(L(q) \cdot m_M(q))}{dq} i \quad (2.35)$$

$$\lambda = L(q)i \quad (2.36)$$

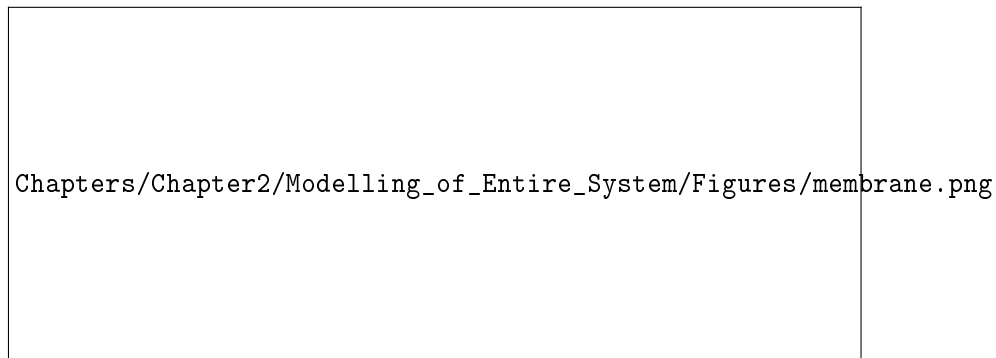


FIGURE 2.14: Membrane structure of the last prototype.

This membrane is a simple Celtic-cross structure made of thin silicone integrated with the entire structure of the device, the membrane is built with a central cylindrical chamber used to trap the magnet in the center of the cross.

The membrane can be modeled as a mass-spring-damper system.

### Membrane stiffness

The membrane stiffness can be calculated using Young's modulus of the material and the geometry of the membrane. Each arm of the cross can be considered as a cantilever beam, the stiffness of a cantilever beam can be calculated as:

$$k_s = \frac{3EI_x}{L^3} \quad (2.37)$$

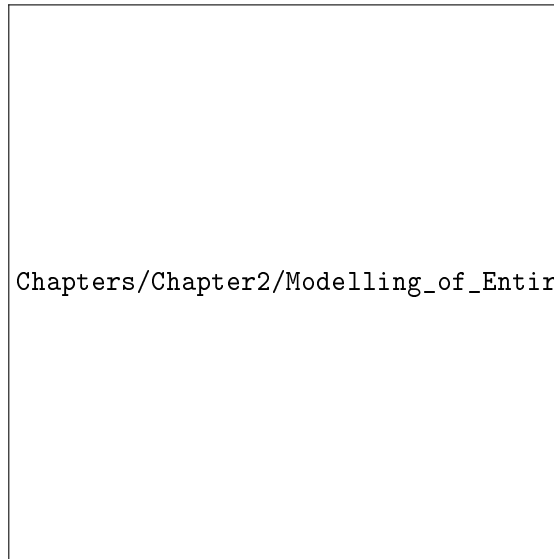
Where:

- $ks$  is the stiffness of the membrane's arm [N/m]
- $E$  is the Young's modulus of the material [Pa]
- $I$  is the second moment of inertia of the arm [m<sup>4</sup>]
- $L$  is the length of the arm [m]

The arm can be simplified as a parallelepiped with a rectangular section, and the second moment of inertia on x can be calculated as:

$$I_x = \frac{wt^3}{12} \quad (2.38)$$





Chapters/Chapter2/Modelling\_of\_Entire\_System/Figures/4\_arms\_springs.png

FIGURE 2.17: Membrane arms parallel springs.

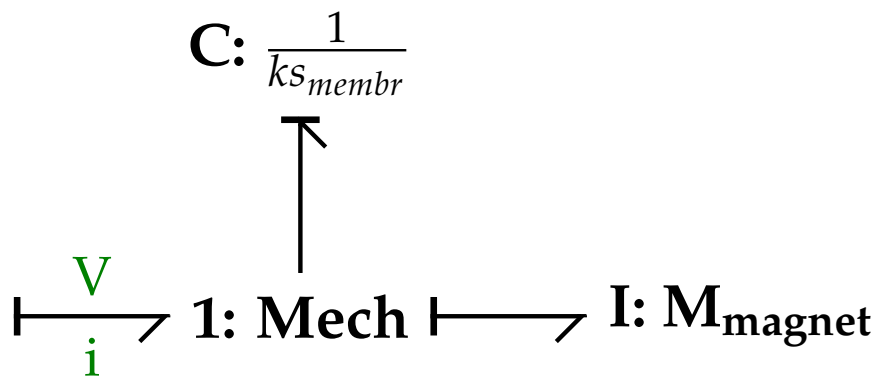


FIGURE 2.18: Final mechanical bond-graph of the membrane and magnet.

Where:

- $I_x$  is the second moment of inertia on the x-axis [ $\text{m}^4$ ]
- $w$  is the width of one membrane arm as in figure 2.14[m]
- $t$  is the thickness of the membrane as in figure 2.14[m]

Then we can consider the 4 arms as 4 springs in parallel, the total stiffness of the membrane can be calculated as:

$$k_{s_{membr}} = 4ks \quad (2.39)$$

### Membrane damping

The damping for a cantilever beam is neglectable, so we can remove the resistive component from the mechanical model.

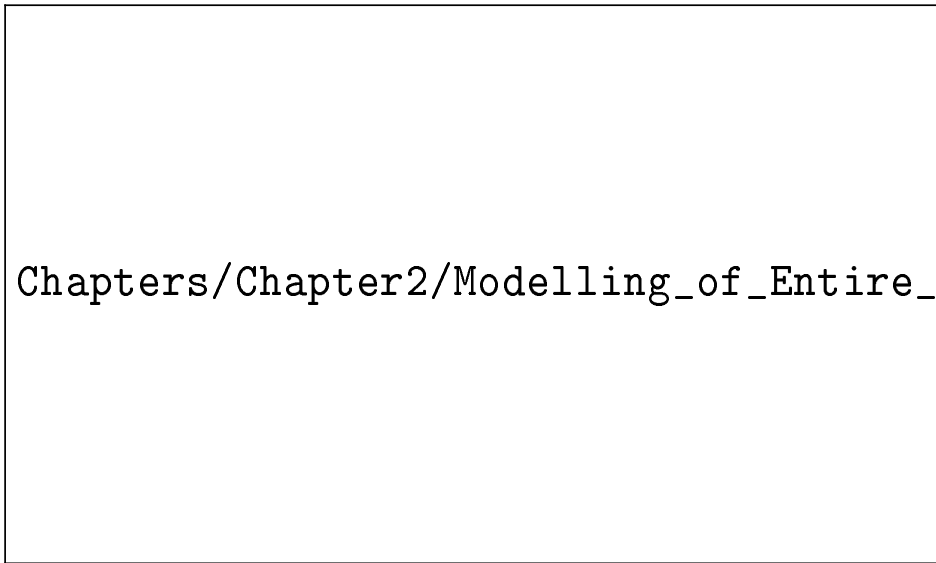


FIGURE 2.19: Model of two soft fingers grasping the object.

#### 2.4.4 Finger grasping model

At last, we have also to model the finger grasping the device, we can derive the model from the one used in [13] for the human finger.

This model describes two fingers grasping an object, for our case, we can simplify it to a single finger grasping the device. Also, we can neglect the friction between the finger and the device as the device will be tested positioned on a flat surface with only the finger touching it from above.

### 2.5 Membrane-Finger haptic system

#### 2.5.1 Introduction on haptic feedback

#### 2.5.2 Transfer of Energy between membrane and finger

#### 2.5.3 Magnetic strenght and Kinetic Energy

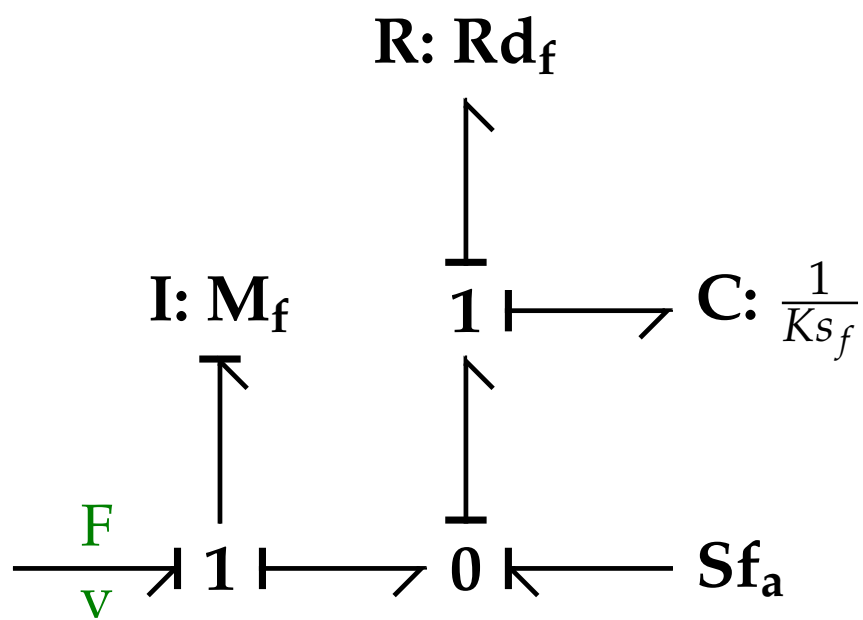
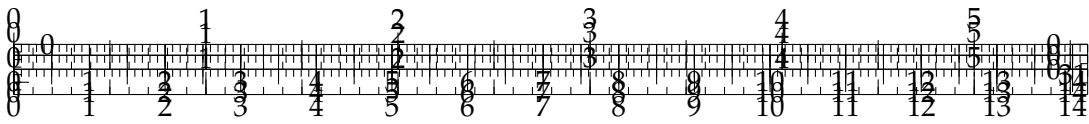


FIGURE 2.20: Bond graph of the finger grasping model.





## Chapter 3

# Overview of Haptic Feedback

### 3.1 Introduction to Haptic Feedback

#### 3.1.1 Vibration Propagation in the finger's pulp

### 3.2 Piezoelectric actuators

#### 3.2.1 Force performances

Traditional pose estimation techniques usually use hand-crafted landmarks detectors and descriptors e.g. SIFT, SURF, MSER and BRIEF. These features serve as anchor points for establishing correspondences between 2D and 3D space, then estimate the pose using non-linear optimisation from the correspondence set. The landmarks are detected automatically and described using heuristic measures of geometric and photometric invariance.

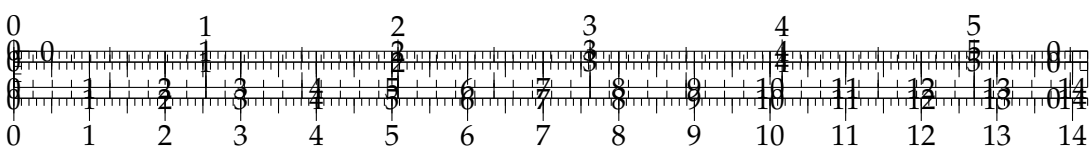
#### 3.2.2 Frequency response

Robust algorithms like Random Sample Consensus (RANSAC) [6] play a pivotal role in filtering out outliers and estimating pose accurately. It is a robust algorithm widely used in computer vision and geometry computations for model fitting. As presented in [18], its primary objective is to estimate parameters of mathematical model from a set of observed data contaminated with outliers. RANSAC achieves this by iteratively selecting random subsets of data points, fitting a model to each subset, and identifying the consensus set of inliers that agree the model.

After the random selection of a minimal subset of data points, the model is fitted to the randomly selected subset. The type of model depends on the specific application, such as lines, planes or more complex structures. The model is then used to classify the remaining data points as inliers or outliers based on a predefined threshold. Data points that fit the model within the threshold are considered inliers.

The process is repeated from a fixed number of iterations, and the model with the largest consensus set (the set of inliers) is retained. With the consensus set, the model is refined using all inliers, and the final model parameters are obtained.

However, this method is susceptible to changes in lighting conditions and large variations in pose and texture. Nonetheless, the earlier research has given birth to effective and well-understood geometric algorithms (e.g. PnP solvers) that are able to estimate the pose accurately and robustly, given a reasonable correspondence set.



### 3.2.3 Powering circuits

SfM [36] represents a powerful paradigm for reconstructing the three-dimensional structure of a scene from a sequence of two-dimensional images. It assumes that the scene consists of static objects, and the motion is captured by the movement of the camera. SfM simultaneously estimates the camera poses and the 3D structure of the scene. Bundle Adjustment is a fundamental optimization technique within SfM, iteratively refining camera poses and the associated 3D structure. This approach is particularly effective in scenarios with sequential image captures, as seen in applications like photogrammetry.

Firstly distinctive features, such as keypoints, are extracted from each image in the sequence and matched together, establishing 2D-2D or 2D-3D correspondences. The camera poses for each image are estimated using techniques like Perspective-n-Point (PnP) algorithms [17]. The 3D coordinates of the scene points are mapped with a triangulation technique using the established correspondences and camera poses. Lastly the camera poses and 3D points are jointly refined to minimize the reprojection error across all images.

SfM is widely applied in applications such as creating 3D models of structures, objects, or scenes from a collection of images. It contributes to the alignment of virtual and real-world elements in augmented reality applications.

### 3.2.4 WeArt implementation

Motivated by the success of deep learning in image classification and object detection, end-to-end learning methods for pose estimation have emerged ([32], [2], [11]). The advent of convolution neural networks (CNN) has revolutionized pose estimation by enabling the automatic learning of hierarchical features from images. These networks can be applied for end-to-end pose regression or integrated into larger systems. Their adaptability makes them suitable for real-time systems and object tracking.

These approaches utilize CNN architectures to learn complex non-linear mappings from input images to output poses. However, despite these end-to-end methods have demonstrated some success, they not achieved similar accuracy as geometry-based solutions.

PoseNet [12] is a pioneering deep learning architecture designed for estimating the camera pose directly from images. It reframes the pose estimation problem as a regression task, predicting both translation and rotation parameters.

The network architecture typically includes convolutional layers for feature extraction followed by fully connected layers for regression.

This approach is valuable in applications where real-time translation and rotation information are critical. However, the training process becomes more complex as diverse datasets are required for effective model generalization.

Mask R-CNN [8] represents a fusion of object detection and instance segmentation, providing detailed pose information for each detected object. In addition to identifying objects in image, it provides detailed information about the shape and location of each instance, making it suitable for accurate pose estimation.

The model extends the Faster R-CNN architecture by incorporating an additional branch for predicting masks. This enables precise delineation of object boundaries,

contributing to improved pose estimation, especially in scenario with complex object shapes.

This architecture is particularly effective in scenarios where precise delineation of object boundaries is essential. However, its computational demands are higher compared to simpler architectures.

Networks designed for hand-eye coordination focus on tasks where precise pose estimation is critical for robotic manipulation. These networks contribute to the seamless interaction between robotic arms and surrounding environment.

These networks often involve architectures tailored for the specific requirements of robotic systems, combining vision-based pose estimation with control algorithms. They play a crucial role in applications such as robotic grasping and object manipulation.

Challenges often arise due to limited data availability for specific tasks, requiring careful consideration during model development.

Even though the above described methods have demonstrated some success, they have not achieved similar accuracy as geometry-based solutions. Indeed, recent work [27] suggests that *"absolute pose regression approaches are more closely related to approximate pose estimation via image retrieval"*, thus they may not generalise well in practise.

While the keypoint matching problem can be solved with machine learning, feature learning methods based on deep convolutional neural networks (CNNs) typically fix 2D-3D keypoints associations and learn to predict the image locations of each corresponding 3D landmark. Examples include studies such as [25], [24] and [34], which mainly differ in model architecture and the choice of keypoints. For instance, [24] employs semantic keypoints, while [34] opts for vertices of the 3D bounding box.

In this spaceborne scenario, objects are typically not occluded and have relatively rich texture. As a result, it was opted for object surface landmarks in order to better relate them to strong visual features.

A notable commonality among these CNN-based methods is their shared characteristic of gradually transforming feature maps from high-resolution representations to low-resolution ones, then recovering them to high-resolution representations later in the process. Recent research emphasizes the significance of maintaining a high-resolution representation throughout tasks like object detection and human pose estimation [30][31]. Specifically, the High-Resolution Net (HRNet) [30], illustrated in figure 3.1, upholds a high-resolution representation while exchanging information across parallel multi-resolution subnetworks, yielding superior spatial precision in landmark heatmaps. In the implemented satellite pose estimation framework, HRNet is leveraged to predict the locations of 2D landmarks in each image, contributing to achieving state-of-the-art accuracy.

HRNet is a CNN with parallel high-to-low resolution subnetworks with repeated information exchange across multi-resolution subnetworks (multi-scale function) implemented for human pose estimation, aiming to detect the locations of  $K$  keypoints or parts of the human body from an image.

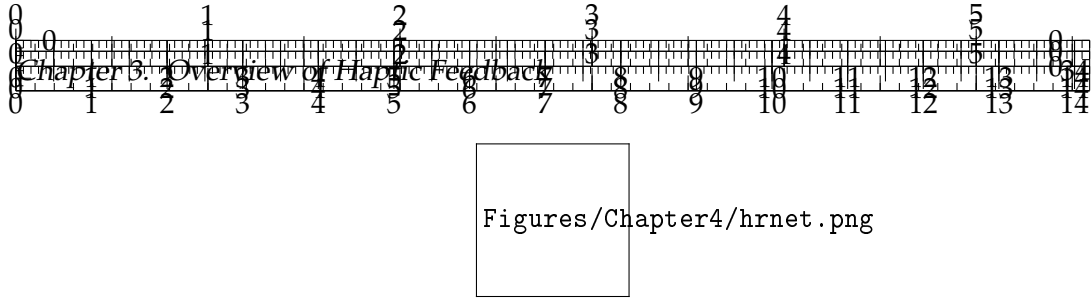


FIGURE 3.1: HRNet Architecture. The horizontal and vertical directions correspond to the depth of the network and the scale of the feature maps, respectively.

The architecture consists in two strided convolutions decreasing the resolution, a main body outputting the feature maps with the same resolution as its input feature maps, and a regressor estimating the heatmaps where the keypoints are chosen and transformed to the full resolution, see figure 3.1.

Existing pose estimation networks are typically constructed by connecting subnetworks of varying resolutions in a sequential manner. Each subnetwork, representing a stage, comprises a series of convolutional layers, and there is a down-sampling layer between adjacent subnetworks to reduce the resolution by half. Let's denote  $N_{sr}$  as the subnetwork in the  $s$ th stage, with  $r$  indicating the resolution index (where its resolution is  $\frac{1}{2^{(r-1)}}$  times lower than that of the first subnetwork). In a high-to-low network with  $S$  stages, such as 4 stages, it can be represented as:

$$N_{11} \rightarrow N_{22} \rightarrow N_{33} \rightarrow N_{44}. \quad (3.1)$$

*HRNet* proposes a parallel multi-resolution subnetwork approach, starting with a high-resolution subnetwork as the initial stage. Subsequently, high-to-low resolution subnetworks are gradually added one by one, creating new stages, and connecting these multi-resolution subnetworks in parallel. As a result, the resolutions for the parallel subnetworks in a later stage consist of the resolutions from the previous stage, along with an extra lower one.

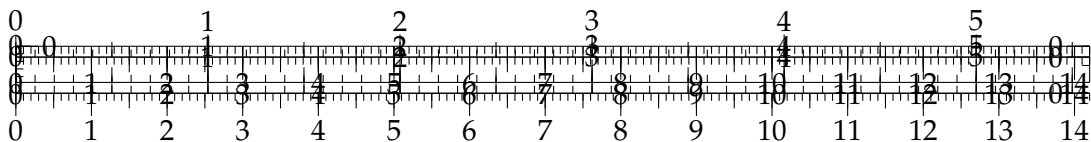
An example network structure (with 4 parallel subnetworks) is given as follows:

$$\begin{aligned} N_{11} &\rightarrow N_{21} \rightarrow N_{31} \rightarrow N_{41} \\ &\searrow N_{22} \rightarrow N_{32} \rightarrow N_{42} \\ &\quad \searrow N_{33} \rightarrow N_{43} \\ &\quad \quad \searrow N_{44} \end{aligned} \quad (3.2)$$

Exchange units are introduced across parallel subnetworks, enabling each subnetwork to repeatedly receive information from other parallel subnetworks. An example illustrates this information exchange scheme. In this example, the third stage is divided into several (e.g., 3) exchange blocks, with each block composed of three parallel convolution units. These parallel units are connected through exchange units, as shown below:

$$\begin{aligned} C_{131} &\searrow \quad \nearrow C_{231} \searrow \quad \nearrow C_{331} \searrow \\ C_{132} &\rightarrow E_{13} \rightarrow C_{232} \rightarrow E_{23} \rightarrow C_{332} \rightarrow E_{33} \\ C_{133} &\nearrow \quad \searrow C_{233} \nearrow \quad \searrow C_{333} \nearrow \end{aligned} \quad (3.3)$$

Here,  $C_{bsr}$  represents the convolution unit in the  $r$ -th resolution of the  $b$ -th block in the  $s$ -th stage, and  $E_{bs}$  is the corresponding exchange unit.



The exchange unit aggregates the inputs, which are  $s$  response maps:  $\{X_1, X_2, \dots, X_s\}$ , to produce  $s$  response maps as outputs:  $\{Y_1, Y_2, \dots, Y_s\}$ , where the resolutions and widths remain consistent with the inputs. Additionally, an extra output map  $Y_{s+1}$  is generated by the exchange unit across stages:  $Y_{s+1} = a(Y_s, s + 1)$ .

The function  $a(X_i, k)$  in this context includes upsampling or downsampling operations on  $X_i$  from resolution  $i$  to resolution  $k$ . Downsampling is achieved through strided  $3 \times 3$  convolutions, such as a single  $3 \times 3$  convolution with a stride of 2 for  $2 \times$  downsampling, or two consecutive strided  $3 \times 3$  convolutions with a stride of 2 for  $4 \times$  downsampling. For upsampling, nearest neighbor sampling is followed by a  $1 \times 1$  convolution to align the number of channels. When  $i = k$ ,  $a(\cdot, \cdot)$  represents an identity connection, and  $a(X_i, k)$  is equivalent to  $X_i$ .

In the implemented method, the original architecture has been slightly modified in order to match the specifics of the analyzed case (grayscale  $512 \times 512$  images).

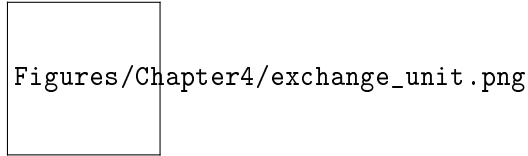


FIGURE 3.2: Exchange unit. Right legend: strided  $3 \times 3$  = strided  $3 \times 3$  convolution, up samp.  $1 \times 1$  = nearest neighbor up-sampling following a  $1 \times 1$  convolution.

Monocular spacecraft pose estimation techniques typically embrace a model-based strategy. For instance, in studies like [5] and [29], the initial step involves image pre-processing and the utilization of feature detectors to identify salient features like line segments and basic geometric shapes. Subsequently, search algorithms are deployed to establish appropriate matches between the detected features and the 3D structure. Poses are then computed using Perspective-n-Point (PnP) solvers such as EPnP [17], and refinement is carried out through optimization techniques.

As outlined in section 4, the implemented approach also generates 2D-3D correspondences; however, along with the coordinates of 2D landmarks, they are regressed using a trained deep network.

The Spacecraft Pose Network (SPN) [28] represents a crucial contribution to the spacecraft project estimation problem using deep learning methods. SPN employs a hybrid of classification and regression neural networks for solving the pose estimation problem. Initially, it predicts the bounding box of the satellite in the image using an object detection sub-network. Subsequently, a classification sub-network retrieves the  $n$  most relevant base rotations from the feature map of the detected object. The regression sub-network learns a set of weights and produces the predicted rotation as a weighted average of the  $n$  base rotations. Finally, SPN determines the relative translation of the satellite by leveraging constraints derived from the predicted bounding box and rotation (for more comprehensive overview of spacecraft pose estimation, please read [3]).

Iterative Closest Point (ICP) [1] is a popular algorithm used for aligning two sets of 3D points through an iterative optimization process. It is commonly employed in scenarios where a reference 3D model needs to be aligned with a partially observed

or reconstructed 3D scene. ICP iteratively refines the transformation between the two point sets to minimize the distance between corresponding points.

An initial transformation (translation and rotation) between the two point sets is estimated. the correspondences between the points in the reference and observed sets are established based on proximity, a weighted least-squares approach is used to minimize the distance between corresponding points, giving higher importance to reliable matches and the transformation is updated based on the registration results. The process is repeated iteratively until convergence, with a check for the change in transformation parameters.

Coherent Point Drift (CPD) [20] is a sophisticated mathematical technique used in the field of point cloud registration. The primary goal of CPD is to align one point cloud with another, ensuring that they match as closely as possible. This alignment is particularly useful when working with objects or scenes that undergo only rigid transformations, meaning that they can be translated and rotated without deformation.

CPD takes a unique approach by treating the point clouds as probability distributions. Each point in the source and target clouds is associated with a probability density. In essence, the source points represent samples from one distribution, and the target points represent samples from another. This probabilistic perspective allows CPD to find optimal correspondences between points in the source and target clouds.

Given two point sets  $X = \{x_1, x_2, \dots, x_N\}$  and  $Y = \{y_1, y_2, \dots, y_M\}$  and initial point correspondences unknown, the estimation of the transformation is achieved through an optimization process with the objective of finding the optimal rigid transformation parameters to align  $X$  with  $Y$ .

#### Mathematical Steps:

- **Initialization:** the transformation parameters:  $R$  (rotation matrix) and  $t$  (translation vector) are initialized.
- **Expectation-Maximization (EM) Iterations:**
  - **E-step (Expectation Step):** computes the soft correspondences between points in  $X$  and  $Y$  using a Gaussian Mixture Model (GMM) with only rigid transformations. The probability of correspondence  $P_{ij}$  between  $x_i$  and  $y_j$  is calculated based on the distance between transformed  $x_i$  and  $y_j$  using the current  $R$  and  $t$ .

$$P_{ij} = \frac{\exp\left(-\frac{1}{2\sigma^2}\|R \cdot x_i + t - y_j\|^2\right)}{\sum_{k=1}^M \exp\left(-\frac{1}{2\sigma^2}\|R \cdot x_i + t - y_k\|^2\right)} \quad (3.4)$$

- **M-step (Maximization Step):** Updates the rotation matrix  $R$  and translation vector  $t$  based on the soft correspondences. It uses a closed-form solution to compute the optimal rotation and translation.

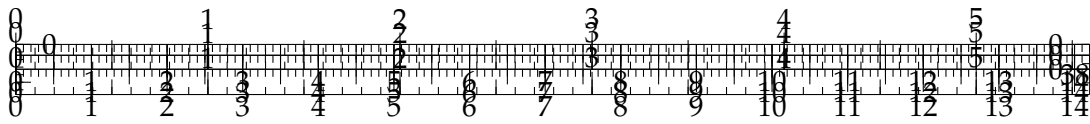
$$R, t = \arg \min_{R, t} \sum_{i=1}^N \sum_{j=1}^M P_{ij} \|R \cdot x_i + t - y_j\|^2 \quad (3.5)$$

- **Convergence Check:** It checks for convergence by examining the change in the transformation parameters between consecutive iterations. If the parameters converge or a maximum number of iterations is reached, the algorithm terminates.
- **Output:** The final rotation matrix  $R$  and translation vector  $t$  represent the rigid transformation aligning  $X$  with  $Y$ .

The Gaussian Mixture Model (GMM) is used to assign soft correspondences, allowing the algorithm to handle cases where points in one set do not have clear one-to-one correspondences with points in the other set. The algorithm iteratively refines the transformation parameters until convergence.

As outlined in section 4.3.2, this approach is used in the implemented method to refine the final pose by the predicted 3D landmarks position.

### 3.3 Performance comparison between Piezo and Coil's actuators



## Chapter 4

## Powering circuit design

#### 4.0.1 Power Circuit Block diagram

## 4.1 Controller

Figure 4.1 describes the overall offline pipeline of the implemented methodology, which consists of several main modules.

From the satellite CAD model nine landmarks have been manually selected (details about the selection criteria explained in section 4.5.1). The 2D-3D correspondence of each landmark is used for training the *Landmark regression* module to predict the nine landmarks image position and the *Landmark Mapping* module to reconstruct the 3D position of each landmark from their image position. The implemented code can be accessed in [19].

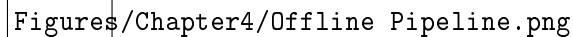


FIGURE 4.1: Offline pipeline of the implemented pose estimator.

### 4.1.1 ESP32 waveform generator for a single module

## Controller code

## Esp32 DAC limitations

## Esp32 DAC Noise

The computation of the 3D position of landmarks in the training images involves a transformation process that leverages the relative positions of the selected landmarks with respect to the satellite’s reference system, as well as the position and orientation of the camera.

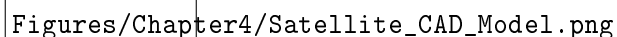
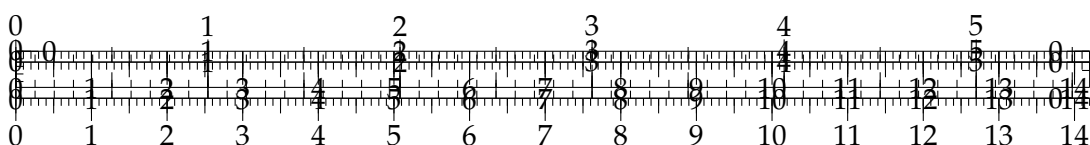


FIGURE 4.2: Selected Landmarks on the CAD Model.





The 3D landmarks are defined in the context of the satellite's reference system. These landmarks represent specific features on the satellite's structure. Their 3D coordinates are known relative to the satellite's own coordinate system thanks to the CAD model.

The camera that captures the training images is mounted on the wrist of a robotic arm on the servicer satellite and its position and orientation with respect to the satellite's reference system is paired with images in the training dataset.

To determine the 3D position of the landmarks in the camera's coordinate system, a simple operation is performed, transforming the landmarks' positions from the satellite's frame to the camera's frame by means of the systems' transformation matrix.

$$x_{cam,i} = \begin{bmatrix} \mathbf{R}^T & t_{c,s} \\ 0 & 1 \end{bmatrix} x_{sat,i} \quad i = 1, \dots, N \quad N : \text{number of landmarks} \quad (4.1)$$

Furthermore, perspective projection transformation (described in section ??) is performed, relating 3D world coordinates  $\{x_i\}$  to 2D image coordinates  $\{z_i\}$  by means of the perspective matrix  $\{\mathbf{P}\}$ .

$$z_i = \mathbf{P} * x_{cam,i} \quad i = 1, \dots, N \quad (4.2)$$

Each training image is first pre-processed (description of the pre-processing process in section 4.3.1) and then coupled with a set of ground truth 2D landmarks  $\{z_i\}$ , as described in section 4.1.1. Those labels are used to supervise the training of the regression model to predict the 2D position of landmarks in the testing images. An additional label is introduced to handle images that capture only partially the satellite, the visibility coefficient  $\{v_i\}$ .

$$v_i = \begin{cases} 1, & \text{if } z_i \text{ is inside image frame.} \\ 0, & \text{otherwise.} \end{cases} \quad (4.3)$$

The output of the model is a tensor of 9 heatmaps, one for each landmark  $h(z_i^p)$ . The ground truth heatmaps  $h(z_i)$  are generated as 2D normal distributions with mean equal to the ground truth location of each landmark, and standard deviation of 1-pixel (code in appendix A.1).

The model is trained from scratch by minimizing the following customized loss:

$$l = \frac{1}{N} \sum_{i=1}^N v_i (h(z_i^p) - h(z_i))^2 \quad (4.4)$$

The loss function  $l$  is defined on a single image and in a mini batch  $l$  is simply averaged. The model is trained in 100 epochs with the *Adam optimizer*[14].

In order to select the landmark location in the predicted heatmap, an additional selection algorithm is introduced.

Each predicted heatmap is normalized over  $[-1,+1]$  range, where  $-1$  represents a totally black pixel and  $+1$  totally white. After an accurate study on the heatmaps that presents an accurately predicted landmark, the main result is that most of those images presented maximum value  $> -0.5$ , so a first threshold  $t_1$  is introduced and set to that value. In only few cases the prediction of the landmark is more imprecise, due, for instance, to similarities with other features in the image. For those cases a second lower threshold is included  $t_2 = -0.6$ .

Firstly pixels in the images with value lower than  $t_2$  are by default set to black ( $-1$ ) to clear the image from impurities, then, for those heatmaps with maximum value over  $t_1$ , the position of their maximum value is taken as landmark position. On the other hand, for those who present a maximum value within the thresholds  $t_1$  and  $t_2$  an additional check on the heatmap variance is performed: only for those with a variance value over  $2e^{-6}$  the landmark is considered within the image and its location is registered as above. For all the other heatmaps that do not follow these conditions, the landmark is considered out of the image frame (2D location set to default value  $[-1,-1]$ ) and the visibility coefficient  $v_i$  is set to zero.

In case of visually similar landmarks, an additional check is introduced. The position of a landmark registered after recognition is compared with the previously registered landmarks. In case it has a position within a certain pixel range near to another landmark, the one with higher maximum value and variance is registered and the other is considered out of frame (code in appendix A.2). Figure 4.3 shows the algorithm's identification process.

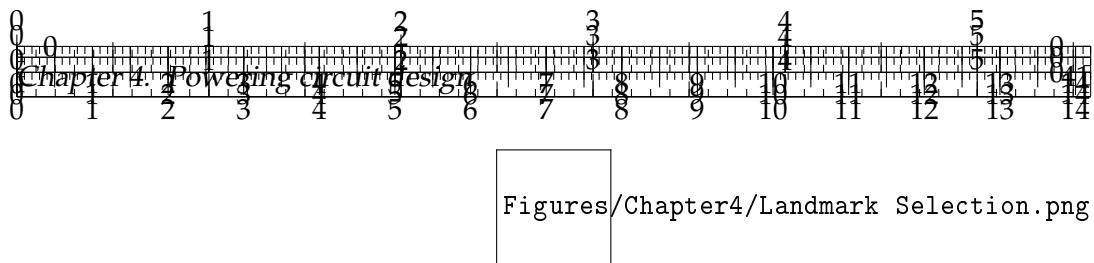


FIGURE 4.3: Landmark Identification Algorithm.

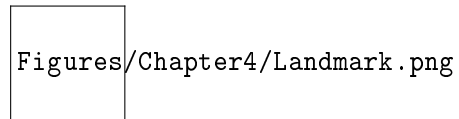


FIGURE 4.4: Landmarks identified by the Landmark Regression module.

The Landmark Mapping is a neural network designed to estimate the 3D positions of landmarks using their 2D positions, mapping the 2D-3D relation. The network takes as input the 2D positions of landmarks obtained from the Landmark Regression module (4.1.1) and predicts as output the respective 3D position.

The network has two hidden layers:

- The first hidden layer consists of 128 units. It processes the input data and learns complex patterns and relationships between the 2D and 3D coordinates.
- The second hidden layer has 64 units and further refines the features learned in the previous layer.

ReLU activation functions are applied after the first and second hidden layers. ReLU introduces non-linearity and helps the network capture complex relationships in the data.

The output layer is responsible for regressing the 3D positions of the landmarks. Each landmark is represented by a 3D coordinate (x, y, z). The output layer produces these 3D coordinates for all the landmarks.

The output of the network is reshaped to organize the predicted 3D coordinates for each landmark. This reshaping ensures that the output is in a format suitable for further processing.

The model is trained with the 2D-3D correspondences described in section 4.1.1, but, before training, the 3D ground truth of landmarks out of image frame ( $v_i = 0$ ) is set to default value  $[0, 0, 0]$ .

The model is trained from scratch by minimizing the following loss:

$$l = \frac{1}{N} \sum_{i=1}^N v_i (\mathbf{x}_i^p - \mathbf{x}_i)^2 \quad (4.5)$$

In the above equation the  $\mathbf{x}_i^p$  represents the 3D position of the  $i$ -th landmark predicted by the model, while  $\mathbf{x}_i$  is its ground truth position.

As in the previous model, the loss function  $l$  is defined on a single group of landmarks and in a mini batch it is simply averaged. The model is trained in a maximum of 150 batches with a *Adam optimizer*[14].

In order to improve the accuracy of the algorithm, three models are created, each of them specialized in a specific range of distance from the target. The training dataset is so split in three subdatasets depending on the distance on the z axis from the satellite with a 100 images superposition per model from each trajectory. The table below shows the specifications of each model.

Model Name	Covered Range (m)
M1	2.00-1.20
M2	1.40-0.50
M3	0.70-0.40

TABLE 4.1: Specifics of three models  $M1$ ,  $M2$  and  $M3$ .

In order to prevent overfitting, an *Early Stopping* algorithm [9] has been introduced. Overfitting occurs when a neural network becomes too specialized in its understanding of the training data, to the point that it struggles to generalize to new,

unseen data. The idea behind early stopping is to maintain under control the network's performance, particularly on a separate dataset called validation set, as it undergoes training. During the training process, the neural network works on refining its parameters using the training dataset. But instead of letting it train tirelessly until convergence, the training process is periodically paused and its performance are evaluated on the validation set. If, over a certain number of consecutive evaluations (determined by a parameter known as "patience"), the network's performance starts to worsen, it's an early warning sign. It suggest that the model is becoming too specialized. Once the point where the validation performance is consistently declining, the training phase is stopped. At this moment, the neural network is considered to have reached its optimal performance on unseen data. Its parameters are taken as the final model, capable to generalize to new unseen data.

## 4.2 Signal Conditioning Circuit

### 4.3 Amplifier circuit

The online architecture operates in real-time. It processes the input data from the camera and produces as output the satellite pose estimation.

After being pre-processed, the image captured from the camera is passed to the *Landmark regression* module. The latter predicts the 2D location  $\{z_i\}$  of the 9 landmarks along with the visibility coefficient  $\{v_i\}$  for each of them. The *Landmark Mapping* module then uses these data to compute the 3D position of each landmark with respect to the camera frame. The final 6DOF pose of the satellite is then computed from the CPD module. Figure 4.5 shows the online pipeline of the implemented methodology.

Figures/Chapter4/Online Pipeline.png

FIGURE 4.5: Online pipeline of the implemented pose estimator.

#### 4.3.1 High Power Operational Amplifiers

The image captured from the camera is pre-processed in the *Pre-Processing* module. It consists in a bilateral filter, which is a non-linear, edge-preserving smoothing filter that reduces noise while preserving the edges in an image.

The mathematical steps behind the bilateral filter involve computing weighted averages of pixel values within a local neighborhood.

Figures/Chapter4/bilateral\_filtering.png

FIGURE 4.6: Bilateral Filter mathematical steps.

The formula for the bilateral filter operation can be described as follows:

Given an input image  $I(x, y)$  and the filter parameters:

- $d$  (diameter of each pixel's neighborhood)

- $\sigma_c$  (standard deviation of the color space)
- $\sigma_s$  (standard deviation of the spatial space)

The filtered output image  $B(x, y)$  can be computed using the following equation for each pixel  $(x, y)$ :

$$B(x, y) = \frac{1}{W(x, y)} \sum_{(i, j) \in S} I(i, j) \cdot G_c(I(x, y), I(i, j), \sigma_c) \cdot G_s(x, y, i, j, \sigma_s) \quad (4.6)$$

Where:

- $S$  is the neighborhood of pixel  $(x, y)$ , defined by a window of diameter  $d$ .
- $G_c$  is the color similarity term, which measures the similarity in color between pixels  $(x, y)$  and  $(i, j)$  in the color space.
- $G_s$  is the spatial similarity term, which measures the spatial proximity between pixels  $(x, y)$  and  $(i, j)$ .
- $W(x, y)$  is a normalization factor.

The  $G_c$  term is defined as a Gaussian function in the color space:

$$G_c(I(x, y), I(i, j), \sigma_c) = \exp \left( -\frac{\|I(x, y) - I(i, j)\|^2}{2\sigma_c^2} \right) \quad (4.7)$$

The  $G_s$  term is a Gaussian function in the spatial space:

$$G_s(x, y, i, j, \sigma_s) = \exp \left( -\frac{\|(x, y) - (i, j)\|^2}{2\sigma_s^2} \right) \quad (4.8)$$

Figures/Chapter4/Pre-processing.png

FIGURE 4.7: On the left the original sample image from the training dataset, on the right the resultant image after the application of the bilateral filter ( $d = 40, \sigma_c = 40, \sigma_s = 200$ ).

The bilateral filter operates by applying these Gaussian weighting functions to compute the weighted average of pixel values within the defined neighborhood, both in color and spatial spaces, resulting in a smoothed image that preserves edges and details. The filter helps reduce noise while keeping the important structures in the image intact.

## An old type of op-amp

### Power dissipation problems

#### 4.3.2 High Power Voltage Amplifier

As the *Landmark Mapping* module predicts the position of each landmark independently one from the other and so each landmark has its own error over the three axis, the resultant cloud of points is misaligned with respect to the rigid reference position given by the CAD model.

In order to estimate the 6DOF pose of the satellite and in the meantime overcome this misalignment problem a mathematical technique is used: Coherent Point Drift.

Two sets of 3D points are present: one is the "target", which represents the 3D position of the landmarks in the camera frame supposing no translation and no rotation, and the other is "source", which is the 3D position of the predicted landmarks. The "source" point set is only composed by landmarks identified in the image frame ( $v_i = 1$ ). It is important to know that the algorithm's performances strongly depend on the number of points in the set so, with the camera approaching the target, some landmarks are cut from the image frame and consequently the pose estimation accuracy reduces.

Figures/Chapter4/CPD.png

FIGURE 4.8: Iterations of the CPD optimization process.

## 4.4 Power Supply

## 4.5 Implementation problems and possible alternatives

### 4.5.1 Non idealities

The main problem in the implementation of the *Landmark regression* module (4.1.1) is the selection of the landmarks. Selecting meaningful landmarks is a critical first step, requiring a accurate understanding of the satellite's structure. These landmarks must possess distinct characteristics that remain invariant under varying conditions, such as changes in lighting, orientation, or potential occlusions.

The first performed attempt in the selection of the landmarks was composed of 11 landmarks with relevant features in the satellite's structure. Most of those visual features were similar to each others and the resultant heatmap predicted by the CNN for a single landmark was ambiguous among multiple ones. This led to a complicated recognition of the landmark location in the image with complex and heavier algorithms for the 2D position identification.

In both cases the set of landmarks has been selected near the approach target to limit the number of out of frame landmark in closer positions.

#### Stability

#### Phase Shift

#### Noise

(Noise and )

#### Slew-Rate

### 4.5.2 Alternative Amplifiers

Another notable challenge stems from the limited size of available datasets. A smaller dataset poses a risk of overfitting, potentially hindering the model's ability to generalize across diverse scenarios. Addressing this issue requires careful consideration

of data augmentation techniques, introducing various transformations to enhance the model's adaptability.

The dataset used for training present five different orientations on each axis of the satellite during the whole approaching range. The main limitation given by the used dataset is the lack of combined rotations over multiple axis and a wider range of rotation on single axis.

Even though the *Landmark regression* module training is strictly related to the availability of the images, the *Landmarks Mapping* one is totally independent. The 2D-3D correspondence of landmarks used to train the model requires the only relative position of the landmarks from the CAD Model and the perspective matrix to be performed. This means that a possible further step to expand the dataset is to perform several simulations with rotations over multiple axis to create new wider datasets and improve the model performances.

### Current Amplifiers





architectures and strong community support which contributed to a fluid development experience.

PyTorch is an open-source machine learning framework developed by Facebook's AI Research lab (FAIR). Its design philosophy emphasizes flexibility, enabling researchers and practitioners to tailor datasets and training procedures to specific requirements. The flexibility offered by PyTorch manifests in two key areas: custom datasets and custom training/validation phases. PyTorch supports automatic differentiation, making it easier to implement and experiment with complex neural network architectures. Its community, extensive documentation, and seamless integration with hardware accelerators like GPUs contribute to its popularity in both research and production.

PyTorch facilitates the creation of the custom dataset through the `torch.utils.data.Dataset` class.

By inheriting from this class and implementing the `__len__` and `__getitem__` methods, it's been possible to define datasets tailored to data structure and format used. This capability is invaluable when working with diverse data types, such as images or time-series, allowing seamless integration into PyTorch's data loading utilities.

PyTorch's flexibility extends to the training and validation phases, enabling users to define custom training loops, loss functions, and evaluation metrics. This is crucial for experimenting with novel architectures, incorporating domain-specific metrics, or implementing advanced training techniques. The ability to seamlessly integrate custom logic into the training process empowers researchers to push the boundaries of model development.

The deep understanding of this framework and its functionalities has been of primary importance for using third-party models like *HRNet*[30] integrating with a customized dataset and ad hoc training and validation phase.

## Keep the distance from the coil

### Heat dissipation

Pandas is a powerful data manipulation and analysis library for Python. It provides data structures like DataFrames that facilitate the handling of structured data. Pandas excels in data cleaning, manipulation, and exploration tasks, offering a plurality of functions for indexing, merging, grouping, and aggregating data. Its integration with other libraries, such as NumPy, makes it a go-to choice for working with labeled data and time series.

Pandas DataFrames offer a convenient and versatile way to handle tabular data, making them an excellent choice for storing and preprocessing data before creating datasets in PyTorch. The integration between Pandas and PyTorch simplifies the transition from data exploration to model training.

NumPy is a fundamental library for numerical operations in Python. It provides support for large, multi-dimensional arrays and matrices, along with an assortment of high-level mathematical functions to operate on these arrays.

Moreover, NumPy arrays and PyTorch tensors share several similarities, making them interchangeable in many contexts. These similarities contribute to a smooth integration between the two libraries, facilitating data manipulation and interoperability.

The compatibility between NumPy and PyTorch simplifies data exchange and promotes a cohesive workflow in mixed-library environments.

Matplotlib is a versatile 2D plotting library for Python. Seaborn is a statistical data visualization library built on top of Matplotlib. It provides a high-level interface for creating attractive and informative statistical graphics. Seaborn simplifies the process of generating complex visualizations with concise syntax. It is particularly useful for exploring relationships in datasets through specialized plots for categorical data, distribution plots, and regression plots.

All the plots presented in the *Evaluation of Training Dataset (5.4.1)* and in the *Evaluation of Test Datasets (5.4.2)* sections are created using this library.

## 5.3 Flexible Mat Prototypes

### 5.3.1 Design of the membrane

Material stiffness and thickness

Membrane structure vs magnet dimensions

### 5.3.2 Design of the mat

Distance magnet-coil

Coil trap

Production method and structure

### 5.3.3 Design faults and problems

Membrane fragility

Overall system flexibility

Keeping the distance coil-magnet under finger pressure

Production method

## 5.4 Experimentation and Evaluation

The final pose estimation scores are defined according to [15] score definition, which consists in the identification of translation and rotational errors and their respective scores.

The estimated pose of each image is evaluated using a rotation error  $E_R$  and a translation error  $E_T$ . Lets consider  $q^*$  the rotation quaternion ground truth of an image and  $q$  its estimation and, analogously,  $\mathbf{t}^*$  the ground truth translation of an image and  $\mathbf{t}$  the respective estimation.

The orientation error  $E_R$  is calculated as the angular distance between the predicted,  $q^*$  and ground truth true  $q$  unit quaternions, i.e., the magnitude of the rotation that aligns the target body frame with the camera reference frame.

$$E_R = 2\cos^{-1}(|z|) \quad (5.1)$$

where  $z$  is the real part of the Hamilton product between  $q^*$  and the conjugate of  $q$ , i.e.:  $z + c = q^* \cdot \bar{q}$ , and  $c$  is the vector part of the Hamilton product. The translation errors is defined as the magnitude (2-norm) of difference between the ground-truth

( $\mathbf{t}^*$ ) and estimated ( $\mathbf{t}$ ) position vectors from the origin of the camera reference frame to that of the target body frame:

$$E_T = \|\mathbf{t}^* - \mathbf{t}\|_2 \quad (5.2)$$

The rotation score  $S_R$  is the same as  $E_R$ , but in radians, while the translation score  $S_T$  is defined as the translation error  $E_T$  normalized by the ground truth translation:

$$S_T = \frac{\|\mathbf{t}^* - \mathbf{t}\|_2}{\|\mathbf{t}^*\|_2} \quad (5.3)$$

which penalizes the position errors more heavily when the target satellite is closer. The final score is the sum of contributions of both scores.

$$S = S_R + S_T \quad (5.4)$$

Additionally, the implemented method is subjected to iterative assessments after the execution of each module. This approach allows to discern and analyze the specific impact and weight that each individual module exerts on the final error. By dissecting the performance at each stage, we gain valuable insights into the contributions of each module, facilitating a comprehensive understanding of the overall system dynamics and optimization potential.

#### Landmark Regression Evaluation Metric

The *Landmark Regression* module is assessed computing the mean error values, among the set of landmarks identified in the image. The predicted pixel coordinates are compared with the ground truth ones.

$$E_{2D} = \frac{\sum_{i=1}^N (\mathbf{z}_i^* - \mathbf{z}_i)}{N} \quad \text{with } i = 1, \dots, N \text{ landmarks with } v = 1 \quad (5.5)$$

where  $\mathbf{z}_i^*$  is the  $i$ -th landmark's ground truth position,  $\mathbf{z}_i$  is the respective prediction and  $v$  it is the visibility coefficient.

The overall module error is defined as the L2 norm of the computed mean error:

$$E_{CNN} = \|E_{2D}\|_2 \quad (5.6)$$

#### Landmark Mapping Evaluation Metric

The *Landmark Mapping* module is assessed similarly to the previous one, computing the L2 norm on the mean 3D position error of landmarks marked with visibility coefficient  $v = 1$ . The predicted 3D coordinates are compared with the ground truth ones.

$$E_{3D} = \frac{\sum_{i=1}^N (\mathbf{x}_i^* - \mathbf{x}_i)}{N} \quad \text{with } i = 1, \dots, N \text{ landmarks with } v = 1 \quad (5.7)$$

where  $\mathbf{x}_i^*$  is the ground truth position of the  $i$ -th landmark,  $\mathbf{x}_i$  is the respective prediction and  $v$  it is the visibility coefficient.

The overall module error is defined as the L2 norm of the computed mean error:

$$E_{NN} = \|E_{3D}\|_2 \quad (5.8)$$

5.4.1 Heating testing

Two distinct experiments are conducted to comprehensively evaluate the performance of the implemented method. In the first experiment, the method underwent rigorous testing on the training dataset, where it is exposed to known data. This initial experiment serves as a crucial phase for fine-tuning and optimizing the model's parameters.

Single coil in DC

As predictable, as far as the camera gets closer to the target region, the landmark location prediction becomes more granular and accurate.

It is important to notice that the performed experiment takes into account 40 cm as minimum distance from the target. This is due to an accurate results analysis which reports that in closer positions the number of landmarks in the camera frame is not sufficient to predict correctly the pose.

The *Landmark Regression* module reports an average 2D error  $E_{CNN} = 1.38 \pm 0.06$  pixels over the sixteen training trajectories, corresponding to the 0.0027% considering 512x512 images.

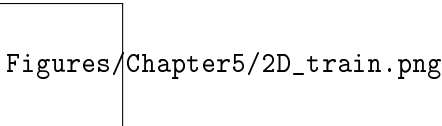


FIGURE 5.1: 2D error over the training dataset.

As it's possible to notice in figure 5.2, the performances are quite the same for each training trajectory, due to the fact that the *Landmark Regression* module predictions are not affected by the orientation of the satellite if this not introduces occlusion. On the other hand the module's performances are strictly affected by the quality and light of the captured image.

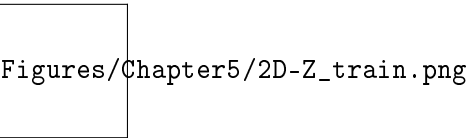


FIGURE 5.2: Landmark Regression error over the trajectory range (z axis) in pixels.

The following table report the mean 2D error and its variance for each trajectory in the train dataset. It's important to notice that the error grows along with the RPY rotations in the respective trajectories (see the trajectories specifics at 1.1).

Trajectory	$E_{CNN}$ [pixels]
TRAY_1	$1.37 \pm 0.05$
TRAY_2	$1.39 \pm 0.05$
TRAY_3	$1.35 \pm 0.06$
TRAY_4	$1.34 \pm 0.06$
TRAY_5	$1.37 \pm 0.07$
TRAY_6	$1.38 \pm 0.07$
TRAY_7	$1.37 \pm 0.06$
TRAY_8	$1.43 \pm 0.06$
TRAY_9	$1.33 \pm 0.06$
TRAY_10	$1.34 \pm 0.06$
TRAY_11	$1.42 \pm 0.07$
TRAY_12	$1.41 \pm 0.05$
TRAY_13	$1.38 \pm 0.05$
TRAY_14	$1.38 \pm 0.05$
TRAY_15	$1.38 \pm 0.05$
TRAY_16	$1.37 \pm 0.05$
Overall	$1.38 \pm 0.06$

TABLE 5.1: Landmark Regression module results.

### Single coil in AC [-V, V]

The evaluation of the performances of *Landmark Mapping* module is performed on both multi-models configuration and single model configuration.

In the first case, each model is trained to cover a specific range of distances from the target. This strategic division aimed to capitalize on the unique strengths of each model within its designated proximity band. The switch between one model to the following one is performed as the predicted distance from the target overcome a threshold for five times.

The following table shows the used thresholds for the models switching:

Models transition	Threshold (m)
M1 $\rightarrow$ M2	1.30
M2 $\rightarrow$ M3	0.60

TABLE 5.2: Thresholds of the multi-model configuration.

The Landmark Mapping module takes the predicted 2D positions of landmarks as input, and as a result, its output is influenced by any residual errors propagated from the preceding module. Notably, the errors in predicting the 3D positions tend to be more pronounced for target locations that are farther from the camera. This happens because a pixel error in the 2D positions at greater distances corresponds to a relatively larger 3D error compared to positions that are closer to the camera.

Figures/Chapter5/Z\_model\_distribution\_train.png

FIGURE 5.3: Models Distribution over thez axis

Figures/Chapter5/3D\_train\_models.png

FIGURE 5.4: Landmark Mapping error for the different models of the multi-model configuration.

Figures/Chapter5/3D\_train\_multi.png

FIGURE 5.5: 3D error over the training dataset in the multi-model configuration.

Figures/Chapter5/3D\_train\_single.png

FIGURE 5.6: 3D error over the training dataset in the single-model configuration.



As it's evident in figures 5.7 and 5.8, the single-model configuration is more consistent than the multi-model one. This is due to the fact that the training phase is performed with a wider dataset than the other configuration, but of diversified data.

The multi-model configuration presents drastic jumps in the transition from one model to another, giving to the switching model algorithm too weight in 3D position evaluation.

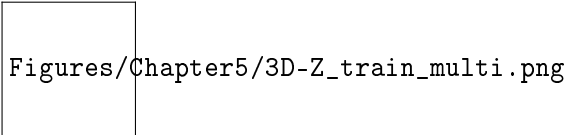


FIGURE 5.7: Landmark Mapping error over the trajectory range (z axis) in the multi-model configuration.

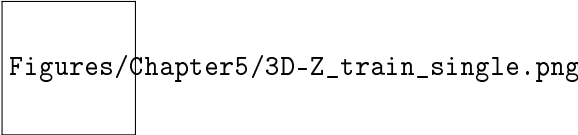


FIGURE 5.8: Landmark Mapping error over the trajectory range (z axis) in the single-model configuration.

Overall the single model configuration presents better performances in the 3D landmarks position prediction. The main problem of the multi-model configuration is the amount of data used to train the three models. With a wider training dataset and a more accurate decision algorithm in the transition from a model to another, this configuration could introduce more robustness in the landmarks position prediction.

In the following table are compared the performances of the two analyzed configuration for each training trajectory.

Trajectory	$E_{NN}$ multi-model	$E_{NN}$ single model
TRAY_1	$(1.02 \pm 0.22)$ cm	$(0.76 \pm 0.22)$ cm
TRAY_2	$(1.06 \pm 0.22)$ cm	$(0.74 \pm 0.22)$ cm
TRAY_3	$(1.02 \pm 0.23)$ cm	$(0.73 \pm 0.23)$ cm
TRAY_4	$(1.05 \pm 0.23)$ cm	$(0.69 \pm 0.23)$ cm
TRAY_5	$(1.16 \pm 0.24)$ cm	$(0.74 \pm 0.24)$ cm
TRAY_6	$(1.30 \pm 0.32)$ cm	$(0.90 \pm 0.30)$ cm
TRAY_7	$(0.87 \pm 0.18)$ cm	$(0.72 \pm 0.18)$ cm
TRAY_8	$(0.82 \pm 0.13)$ cm	$(0.72 \pm 0.13)$ cm
TRAY_9	$(0.86 \pm 0.19)$ cm	$(0.76 \pm 0.19)$ cm
TRAY_10	$(0.91 \pm 0.15)$ cm	$(0.84 \pm 0.15)$ cm
TRAY_11	$(1.03 \pm 0.07)$ cm	$(0.95 \pm 0.07)$ cm
TRAY_12	$(0.94 \pm 0.16)$ cm	$(0.66 \pm 0.17)$ cm
TRAY_13	$(1.03 \pm 0.17)$ cm	$(0.70 \pm 0.17)$ cm
TRAY_14	$(1.31 \pm 0.27)$ cm	$(0.92 \pm 0.27)$ cm
TRAY_15	$(1.59 \pm 0.28)$ cm	$(1.20 \pm 0.28)$ cm
TRAY_16	$(1.90 \pm 0.42)$ cm	$(1.52 \pm 0.42)$ cm
Overall	$(1.12 \pm 0.48)$ cm	$(0.85 \pm 0.35)$ cm

TABLE 5.3: Landmark Mapping module results with single and multi-model configurations.

### Single coil in AC [0, 2V]

The CPD module introduces an ulterior error due to the alignment of the reference points set with the predicted one.

It's important to notice that the two errors  $E_R$  and  $E_T$  are deeply affected by the number of points in the predicted point set.

In cases of a sparse point set, CPD struggles to discern a coherent structure, leading to decreased accuracy in the alignment process. The algorithm's ability to effectively capture the global patterns and deformations decreases, resulting in sub-optimal alignments. Therefore, maintaining an adequate number of points in the input sets is crucial for CPD to deliver robust and reliable performance, ensuring the successful alignment of point clouds in various applications.

Figures/Chapter5/Et-Z\_train\_multi.png

FIGURE 5.9: Translation error over the trajectory range (z axis) in multi-model configuration.

Figures/Chapter5/Et-Z\_train\_single.png

FIGURE 5.10: Translation error over the trajectory range (z axis) in single-model configuration.

Figures/Chapter5/Er-Z\_train\_multi.png

FIGURE 5.11: Rotation error over the trajectory range (z axis) in multi-model configuration.

Figures/Chapter5/Er-Z\_train\_single.png

FIGURE 5.12: Rotation error over the trajectory range (z axis) in single-model configuration.

As shown in figures 5.9 and 5.10, the algorithm performances vary drastically as the number of predicted landmarks becomes six or less.

Trajectory	$E_{CNN}$ (pxls)	$E_{NN}$ (cm)	$E_T$ (cm)	$E_R$ (°)	$S_T$	$S_R$	$S$
TRAY_1	$1.37 \pm 0.05$	$1.02 \pm 0.22$	$2.41 \pm 2.09$	0	0.0228	0	0.0228
TRAY_2	$1.39 \pm 0.05$	$1.06 \pm 0.22$	$2.17 \pm 1.67$	0.010	0.0200	0.0001	0.0201
TRAY_3	$1.35 \pm 0.06$	$1.02 \pm 0.23$	$1.92 \pm 0.98$	0.030	0.0180	0.0005	0.0185
TRAY_4	$1.34 \pm 0.06$	$1.05 \pm 0.23$	$1.89 \pm 0.67$	0.058	0.0170	0.0010	0.0180
TRAY_5	$1.37 \pm 0.07$	$1.16 \pm 0.24$	$2.08 \pm 0.86$	0.095	0.0196	0.0016	0.0212
TRAY_6	$1.38 \pm 0.07$	$1.30 \pm 0.32$	$2.50 \pm 4.91$	0.137	0.0245	0.0024	0.0269
TRAY_7	$1.37 \pm 0.06$	$0.87 \pm 0.18$	$1.96 \pm 1.50$	0.006	0.0185	0.0001	0.0186
TRAY_8	$1.43 \pm 0.06$	$0.82 \pm 0.13$	$1.65 \pm 1.33$	0.022	0.0160	0.0004	0.0164
TRAY_9	$1.33 \pm 0.06$	$0.86 \pm 0.19$	$1.64 \pm 1.48$	0.048	0.0158	0.0008	0.0166
TRAY_10	$1.34 \pm 0.06$	$0.91 \pm 0.15$	$1.71 \pm 1.94$	0.083	0.0167	0.0014	0.0181
TRAY_11	$1.42 \pm 0.07$	$1.03 \pm 0.07$	$1.91 \pm 3.00$	0.127	0.0190	0.0022	0.0212
TRAY_12	$1.41 \pm 0.05$	$0.94 \pm 0.16$	$1.67 \pm 1.88$	0.006	0.0158	0.0001	0.0159
TRAY_13	$1.38 \pm 0.05$	$1.03 \pm 0.17$	$1.55 \pm 1.60$	0.014	0.0138	0.0002	0.0140
TRAY_14	$1.38 \pm 0.05$	$1.31 \pm 0.27$	$2.30 \pm 1.06$	0.023	0.0195	0.0004	0.0199
TRAY_15	$1.38 \pm 0.05$	$1.59 \pm 0.28$	$3.21 \pm 0.70$	0.032	0.0271	0.0005	0.0276
TRAY_16	$1.37 \pm 0.05$	$1.90 \pm 0.42$	$4.23 \pm 0.60$	0.042	0.0357	0.0007	0.0364
Overall	$1.38 \pm 0.06$	$1.12 \pm 0.48$	$2.18 \pm 2.09$	0.046	0.0200	0.0008	<b>0.0208</b>

TABLE 5.4: Results on training set with multi-model configuration.

Trajectory	$E_{CNN}$ (pxls)	$E_{NN}$ (cm)	$E_T$ (cm)	$E_R$ (°)	$S_T$	$S_R$	$S$
TRAY_1	$1.37 \pm 0.05$	$0.76 \pm 0.22$	$2.14 \pm 2.09$	0	0.0196	0	0.0196
TRAY_2	$1.39 \pm 0.05$	$0.74 \pm 0.22$	$1.89 \pm 1.67$	0.010	0.0168	0.0001	0.0169
TRAY_3	$1.35 \pm 0.06$	$0.73 \pm 0.23$	$1.72 \pm 0.98$	0.032	0.0152	0.0005	0.0157
TRAY_4	$1.34 \pm 0.06$	$0.69 \pm 0.23$	$1.66 \pm 0.67$	0.065	0.0152	0.0011	0.0163
TRAY_5	$1.37 \pm 0.07$	$0.74 \pm 0.24$	$1.72 \pm 0.86$	0.110	0.0164	0.0019	0.0183
TRAY_6	$1.38 \pm 0.07$	$0.90 \pm 0.30$	$1.98 \pm 4.91$	0.166	0.0197	0.0029	0.0226
TRAY_7	$1.37 \pm 0.06$	$0.72 \pm 0.18$	$1.93 \pm 1.50$	0.007	0.0174	0.0001	0.0175
TRAY_8	$1.43 \pm 0.06$	$0.72 \pm 0.13$	$1.79 \pm 1.33$	0.028	0.0159	0.0005	0.0164
TRAY_9	$1.33 \pm 0.06$	$0.76 \pm 0.19$	$1.64 \pm 1.48$	0.062	0.0145	0.0011	0.0155
TRAY_10	$1.34 \pm 0.06$	$0.84 \pm 0.15$	$1.55 \pm 1.94$	0.109	0.0131	0.0019	0.0150
TRAY_11	$1.42 \pm 0.07$	$0.95 \pm 0.07$	$1.54 \pm 3.00$	0.168	0.0126	0.0029	0.0155
TRAY_12	$1.41 \pm 0.05$	$0.66 \pm 0.17$	$1.17 \pm 1.88$	0.011	0.0112	0.0002	0.0114
TRAY_13	$1.38 \pm 0.05$	$0.70 \pm 0.17$	$0.85 \pm 1.60$	0.023	0.0083	0.0004	0.0087
TRAY_14	$1.38 \pm 0.05$	$0.92 \pm 0.27$	$1.65 \pm 1.06$	0.036	0.0152	0.0006	0.0158
TRAY_15	$1.38 \pm 0.05$	$1.20 \pm 0.28$	$2.67 \pm 0.70$	0.049	0.0240	0.0009	0.0249
TRAY_16	$1.37 \pm 0.05$	$1.52 \pm 0.42$	$3.75 \pm 0.60$	0.064	0.0335	0.0011	0.0346
Overall	$1.38 \pm 0.06$	$0.85 \pm 0.35$	$1.85 \pm 1.19$	0.058	0.0168	0.0010	<b>0.0178</b>

TABLE 5.5: Results on training set with single-model configuration.

Two coils in parallel DC

Two coils in parallel AC

Tables 5.4 and 5.5 highlight that the single-model configuration demonstrates superior overall performance ( $S = 0.0178$ ) compared to the multi-model configuration ( $S = 0.0208$ ). However, it’s noteworthy that the multi-model configuration has slightly better performance in the rotation aspect despite the overall advantage of the single-model setup.

### 5.4.2 Magnet size vs Force

The second experiment is carried out on a separate test dataset composed of four new and unseen trajectories. This test dataset is intentionally kept independent from the training data, simulating real-world scenarios and ensuring the model’s generalization capabilities. The performance on the test dataset provides insights into the method’s ability to extrapolate learned patterns and accurately handle novel data instances. Together, these two experiments facilitate a comprehensive assessment of the method’s robustness, effectiveness, and generalization across different datasets.

The first two trajectories (*A* and *B*) present an image quality and light conditions similar to the training images, while the other two (*Less\_Difficult\_Trajectory* and *Difficult\_Trajectory*) present light condition too far from the training images and so the system struggles to predict the correct position of each landmarks in the image due to the fact that the *Landmark Mapping* module is quite sensitive to the output of the *Landmark Regression* one. Indeed, if the landmarks that are supposed to be present in the image frame are not all recognised, the 3D landmark position is predicted with high error.

So the system highly relies on the correct identification of each landmark in the image by the *Landmark Regression* (a deepened analysis of the problem and possible improvements is discussed at section 6.3).

Due to this, with the ladder dataset the evaluation is performed only on the *Landmark Mapping* and *CPD* modules, assuming exact the prediction of the landmarks position in the image ( $2D\ Error = 0$ ).

As shown in figures 5.13 and 5.14 the 2D landmarks location is predicted with a good accuracy also on the test set, with an average 2D error  $E_{CNN} = 1.35 \pm 0.04$  pixels (corresponding to the 0.0026% for 512x512 images) and a error variation on the z axis coherent with the training results.

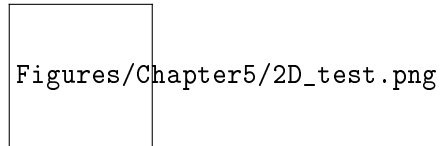


FIGURE 5.13: 2D error over the test dataset.

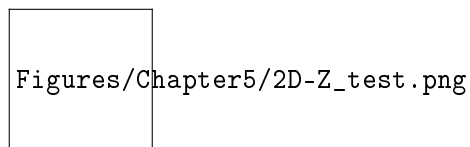


FIGURE 5.14: Landmark Regression error over the trajectory range (z axis) on the test dataset.



In contrast with the training results, the multi-model configuration of the *Landmark Mapping* module express better performances on the test set than the single-model configuration on each test trajectory.

Figures/Chapter5/3D\_test\_multi.png

FIGURE 5.15: Landmark Mapping error in multi-model configuration on test dataset.

Figures/Chapter5/3D\_test\_single.png

FIGURE 5.16: Landmark Mapping error in single-model configuration on test dataset.

In both configurations the *Difficult Trajectory* is predicted with noticeable error in particular in its first part where its RPY rotations are considerable, even beyond the range of rotations known by the models (see figure 5.17 and 5.18).

The EROSS project [26] sets a stringent guideline, aiming to a less than 2-5 centimeters 3D error, reflecting the project's emphasis on precision in spaceborne applications. The achieved 3D error, measured in the experiments, consistently falls within the specified range, showcasing the system's capability to deliver accurate and reliable results, crucial for the success of rendezvous maneuvers and other space missions.

Figures/Chapter5/3D-Z\_test\_multi.png

FIGURE 5.17: Landmark Mapping error over the trajectory range (z axis) in the multi-model configuration on test dataset.

Figures/Chapter5/3D-Z\_test\_single.png

FIGURE 5.18: Landmark Mapping error over the trajectory range (z axis) in the single-model configuration on test dataset.

As previously discussed, the final translation and rotation errors  $E_T$  and  $E_R$  are affected by the number of landmarks in the predicted point set. In figures 5.19 and 5.20, in positions closed to the target, it's possible to see that the translation error increases as far as the number of visible landmarks in the image frame decreases.

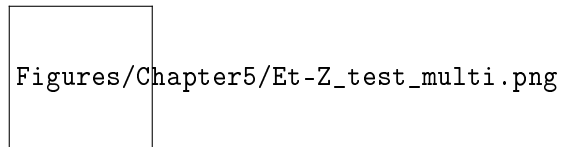


FIGURE 5.19: Translation error over the trajectory range (z axis) in multi-model configuration on test dataset.

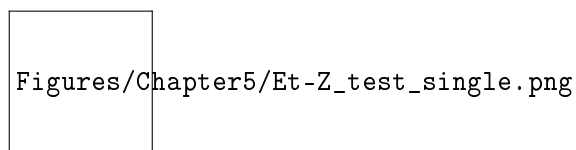


FIGURE 5.20: Translation error over the trajectory range (z axis) in single-model configuration on test dataset.

The multi-model configuration exhibits noticeable performance jumps during the transitions between models. These abrupt shifts highlight the challenge associated with integrating different models, suggesting the need for further refinement in the transition logic to ensure smoother and more consistent predictions across varying proximity bands.

Figures/Chapter5/Er-Z\_test\_multi.png

FIGURE 5.21: Rotation error over the trajectory range (z axis) in multi-model configuration on test dataset.

Figures/Chapter5/Er-Z\_test\_single.png

FIGURE 5.22: Rotation error over the trajectory range (z axis) in single-model configuration on test dataset.

In the following tables are reported the analysed errors and scores for each test trajectory and in both analyzed configurations: multi-model and- single-model.

In contrast to the training results, the single-model configuration has lower performance both on translation and rotation, meaning that compared to the multi-model one demonstrates an overfitting behavior.

Overall, considering the multi-model configuration, the testing performance, both on rotation ( $S_R$ ) and translation ( $S_T$ ), is not so far from the training one and quite encouraging, demonstrating the ability of this configuration to generalize when dealing with unknown data.

Trajectory	$E_{CNN}$ (pxls)	$E_{NN}$ (cm)	$E_T$ (cm)	$E_R$ (°)	$S_T$	$S_R$	$S$
TRAY_A	$1.34 \pm 0.05$	$1.08 \pm 0.29$	2.96	0.601	0.0238	0.0105	0.0343
TRAY_B	$1.37 \pm 0.05$	$1.89 \pm 1.60$	3.62	0.281	0.0287	0.0049	0.0336
Less_D_Tray	$0.00 \pm 0.00$	$1.27 \pm 0.15$	3.32	0.057	0.0337	0.0010	0.0347
Difficult_Tray	$0.00 \pm 0.00$	$5.58 \pm 17.96$	7.73	0.375	0.0697	0.0066	0.0763
Overall	$1.35 \pm 0.04$	$2.46 \pm 8.38$	4.41	0.328	0.0390	0.0057	<b>0.0447</b>

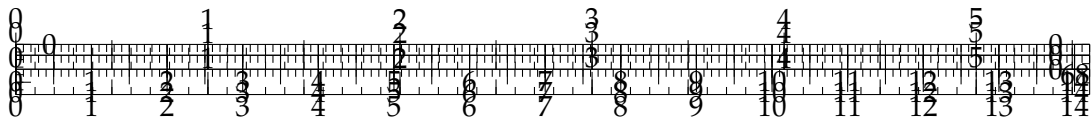
TABLE 5.6: Results on test set with multi-model configuration.

Trajectory	$E_{CNN}$ (pxls)	$E_{NN}$ (cm)	$E_T$ (cm)	$E_R$ (°)	$S_T$	$S_R$	$S$
TRAY_A	$1.34 \pm 0.05$	$0.95 \pm 0.29$	2.04	0.781	0.0165	0.0136	0.0301
TRAY_B	$1.37 \pm 0.05$	$1.21 \pm 1.60$	3.06	0.544	0.0246	0.0095	0.0341
Less_D_Tray	$0.00 \pm 0.00$	$11.76 \pm 0.15$	17.19	0.045	0.1166	0.0008	0.1174
Difficult_Tray	$0.00 \pm 0.00$	$20.69 \pm 17.96$	29.36	0.373	0.2010	0.0065	0.2075
Overall	$1.35 \pm 0.04$	$8.67 \pm 180.0$	12.9	0.435	0.0897	0.0076	<b>0.0973</b>

TABLE 5.7: Results on test set with single-model configuration.

### 5.4.3 Force vs number of coils

### 5.4.4 Voltage vs Force



## Chapter 6

# Discussion and conclusions

### 6.1 Challenges in On-Board AI Systems for Space Missions

AI algorithms in on-board space applications encounter significant challenges related to both verifiability and computational load, crucial factors for the success and safety of space missions.

#### 6.1.1 Verifiability Issues

AI algorithms, particularly those employing deep learning, are characterized by intricate architectures and numerous parameters. The complexity of these models makes it challenging to provide comprehensive assurance of their correctness. In space applications, where system failures are not an option, ensuring the verifiability of AI algorithms becomes predominant.

Many AI models, including deep neural networks, lack inherent explainability. Understanding the decision-making process within these "black box" models is essential to verify their reliability. Achieving transparency in AI decision logic is critical in scenarios where the basis for decision-making must be interpretable, such as during critical space maneuvers.

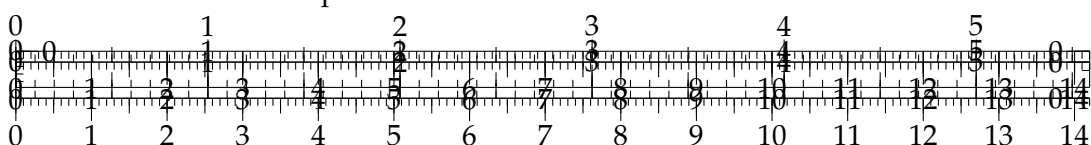
Space environments are dynamic and may exhibit uncertainties. AI algorithms designed for adaptability and learning might introduce challenges in predicting their behavior accurately. Verifying the robustness of adaptive AI systems in the face of unforeseen conditions is a persistent concern.

#### 6.1.2 Computational Issues

On-board space systems typically operate with limited computational resources due to factors such as size, weight, and power constraints (SWaP). Implementing AI algorithms with demanding computational requirements may strain available resources, affecting the overall efficiency of the system.

Certain space applications, such as autonomous navigation or hazard avoidance, demand real-time decision-making. AI algorithms with high computational loads may struggle to meet these stringent timing constraints. Delays in processing could lead to missed opportunities or, in critical situations, mission failure.

In addition to computational power, energy efficiency is a crucial consideration. Prolonged missions and the reliance on energy-harvesting sources necessitate AI algorithms that balance computational complexity with energy consumption, ensuring sustained and reliable operation.



Addressing these challenges requires a multidisciplinary approach involving AI researchers, space engineers, and mission planners. Techniques such as formal verification, explainable AI, and hardware optimization are essential to enhance the verifiability and efficiency of AI algorithms in on-board space applications.

## 6.2 Results Analysis

In the broader context, the multi-model configuration emerges as the more robust and adaptable option, showcasing superior performance on the test set and demonstrating effective generalization capabilities to previously unseen data. The overall system score on the test dataset is  $S = 0.0447$ , primarily affected by the translation component  $S_T = 0.0390$ , as opposed to the relatively lower contribution from the rotation aspect,  $S_R = 0.0057$ . The noteworthy aspect is the necessity of prioritize the minimization of translation errors, since, in proximity to the target, precise translation is crucial for accurate maneuvering. Moreover, rotation pose can be more effectively predicted with the incorporation of a navigation filter. This strategic integration allows for a corrective mechanism, compensating for rotational discrepancies and enhancing the system's overall precision in navigating close quarters.

## 6.3 Possible Improvements

### 6.3.1 Landmark Selection

As already discussed at section 4.5.1, the selection of the number and position of landmarks in the model is crucial for the resulting performances of the system. Since the final translation and rotation errors ( $E_T$ ,  $E_R$ ) are strictly related to the number of landmarks identified in the image frame, which reduces in positions closer to the target, a suitable improvement would be the increase of the initial number of landmarks.

Another option would be using multiple models also for the *Landmark Regression* module, which are able to identify a target set of landmarks in farther positions and a second set in closer distances to the target, in order to keep the number of identified points in the image frame as greater as possible.

This implementation would also lead to a more accurate pose estimation in positions closer to the minimum distance analyzed in the experiments (from 40cm to 20cm). A well-performed pose estimation in positions very close to the target would help to minimize any errors introduced by camera distortions.

### 6.3.2 Landmark Mapping Sensitivity

The assessment of trajectories such as *Less\_Difficult\_Trajectory* and *Difficult\_Trajectory* is conducted with a noteworthy consideration: the assumption of zero prediction error for the points' location in the image. This assumption is made out of necessity since the *Landmark Regression* module encounters difficulties in identifying all the landmarks expected to be present in the image frames. Consequently, the input data for the *Landmark Mapping* module is marked by a heightened sensitivity, as the accuracy of its predictions is contingent upon the successful identification of landmarks by the preceding module.

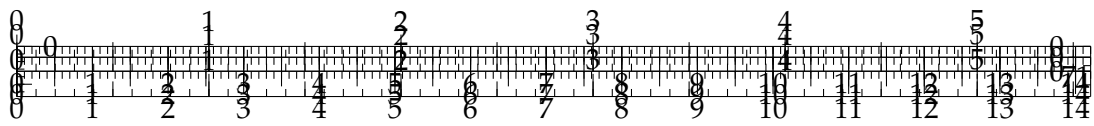
A potential avenue for improvement involves an expansion of the training dataset to incorporate instances where certain landmarks remain unidentified due to inherent challenges in their recognition. This strategy aims to enhance the model's resilience to scenarios where specific landmarks pose persistent issues during identification. By exposing the model to a more diverse range of challenges and including cases of landmark ambiguity, it is anticipated that the trained model will develop a more robust understanding, leading to improved performance, particularly in situations mirroring real-world complexities. This adjustment aligns with the overarching goal of fortifying the system's adaptability and generalization capabilities, addressing challenges posed by varying environmental conditions and unforeseen factors during autonomous space applications.

Moreover, to fortify the robustness of the system, there is a prospect to introduce a more sophisticated pre-processing system. This advanced system would be designed to mitigate the impact of varying image light conditions on landmark identification. By incorporating techniques such as adaptive image enhancement, contrast normalization, or even exploring deep learning-based methods for illumination invariance, the model could become less susceptible to fluctuations in lighting. Such enhancements would foster greater reliability in landmark identification by the *Landmark Regression* module, subsequently improving the overall accuracy of the *Landmark Mapping* module. This proactive approach anticipates and addresses challenges associated with real-world scenarios where illumination conditions can be unpredictable, ensuring the model's effectiveness across diverse operational environments in on-board space applications.

## 6.4 Conclusions

This project presents a dedicated monocular pose estimation framework designed for spaceborne objects, emphasizing its applicability to satellite rendezvous maneuvers. The framework capitalizes on the strengths of deep neural networks, seamlessly integrating feature learning and establishing robust 2D-3D correspondence mapping. Notably, the incorporation of HRNet, known for its high-resolution image representation, significantly contributes to the precision of pose predictions and the subsequent refinement process. The framework further demonstrates its efficiency by employing geometric optimization techniques, ensuring accurate alignment of point sets and enhancing the overall robustness of the pose estimation system.



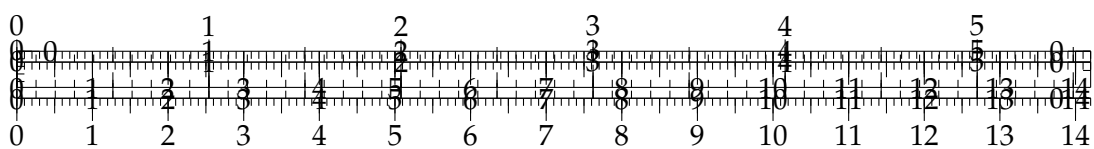


## Appendix A

# Support Code

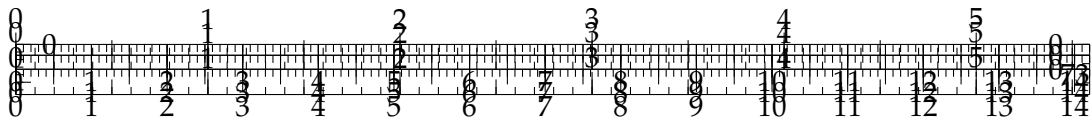
### A.1 Ground Truth Heatmaps

LISTING A.1: Ground Truth Heatmaps



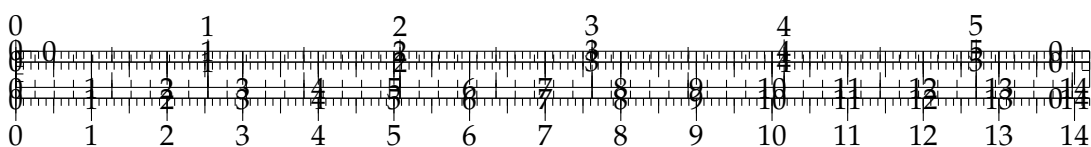
## A.2 Landmark Location Selection

LISTING A.2: Landmark Location Selection

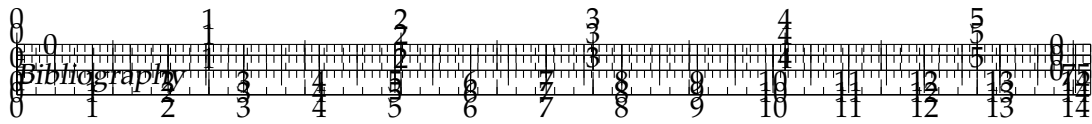


# Bibliography

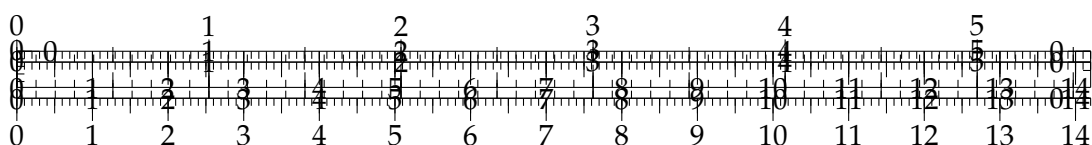
- [1] P.J. Besl and Neil D. McKay. "A method for registration of 3-D shapes". In: *IEEE Transactions on Pattern Analysis and Machine Intelligence* 14.2 (1992), pp. 239–256. DOI: 10.1109/34.121791.
- [2] Samarth Brahmabhatt et al. "MapNet: Geometry-Aware Learning of Maps for Camera Localization". In: *CoRR* abs/1712.03342 (2017). arXiv: 1712.03342. URL: <http://arxiv.org/abs/1712.03342>.
- [3] Pasqualetto Cassinis. "Delft University of Technology Review of the robustness and applicability of monocular pose estimation systems for relative navigation with an uncooperative spacecraft". In: 2019.
- [4] cordis.europa.eu CORDIS. *European Robotic Orbital Support Services: Eross project. Fact sheet: H2020: Cordis: European Commission*. Nov. 2018. URL: <https://cordis.europa.eu/project/id/821904>.
- [5] Simone D'Amico, Mathias Benn, and John Leif Jørgensen. "Pose estimation of an uncooperative spacecraft from actual space imagery". In: 2014. URL: <https://api.semanticscholar.org/CorpusID:1537971>.
- [6] Martin A. Fischler and Robert C. Bolles. "Random sample consensus: a paradigm for model fitting with applications to image analysis and automated cartography". In: *Commun. ACM* 24 (1981). URL: <https://api.semanticscholar.org/CorpusID:972888>.
- [7] Martin Geier et al. "Mathematical Modeling of an Electromagnetic Forming System with Flat Spiral Coils as Actuator". In: (Jan. 2010). DOI: 10.17877/DE290R-14276.
- [8] Kaiming He et al. "Mask R-CNN". In: (2017), pp. 2980–2988. DOI: 10.1109/ICCV.2017.322.
- [9] Jeff Heaton. *T81-558: Applications of Deep Neural Networks*. 2023. URL: <https://sites.wustl.edu/jeffheaton/t81-558/> (visited on 11/27/2023).
- [10] K. Kawabe, H. Koyama, and K. Shirai. "Planar inductor". In: *IEEE Transactions on Magnetics* 20.5 (1984), pp. 1804–1806. DOI: 10.1109/TMAG.1984.1063271.
- [11] Alex Kendall and Roberto Cipolla. "Modelling Uncertainty in Deep Learning for Camera Relocalization". In: *CoRR* abs/1509.05909 (2015). arXiv: 1509.05909. URL: <http://arxiv.org/abs/1509.05909>.
- [12] Alex Kendall, Matthew Grimes, and Roberto Cipolla. "Convolutional networks for real-time 6-DOF camera relocalization". In: *CoRR* abs/1505.07427 (2015). arXiv: 1505.07427. URL: <http://arxiv.org/abs/1505.07427>.
- [13] A. Khurshid, Abdul Ghafoor, and Afzaal Malik. "Robotic Grasping and Fine Manipulation Using Soft Fingertip". In: Aug. 2011. ISBN: 978-953-307-373-6. DOI: 10.5772/23697.
- [14] Diederik P. Kingma and Jimmy Ba. *Adam: A Method for Stochastic Optimization*. 2017. arXiv: 1412.6980 [cs.LG].
- [15] Mate Kisantal et al. "Satellite Pose Estimation Challenge: Dataset, Competition Design and Results". In: *CoRR* abs/1911.02050 (2019). arXiv: 1911.02050. URL: <http://arxiv.org/abs/1911.02050>.

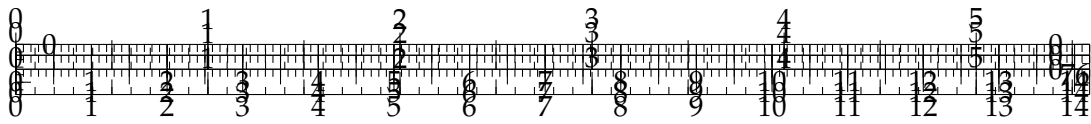






- [33] supermagnete.de. *Magnetic field of various permanent magnets*. <https://www.supermagnete.de/eng/faq/How-do-you-calculate-the-magnetic-flux-density>.
- [34] Bugra Tekin, Sudipta N. Sinha, and Pascal Fua. "Real-Time Seamless Single Shot 6D Object Pose Prediction". In: *CoRR* abs/1711.08848 (2017). arXiv: 1711.08848. URL: <http://arxiv.org/abs/1711.08848>.
- [35] The Engineering ToolBox. *Length of a Spiral*. [https://www.engineeringtoolbox.com/spiral-length-d\\_2191.html](https://www.engineeringtoolbox.com/spiral-length-d_2191.html) [Accessed: 22/04/2024]. 2021.
- [36] Bill Triggs et al. "Bundle Adjustment - A Modern Synthesis". In: *Proceedings of the International Workshop on Vision Algorithms: Theory and Practice*. ICCV '99. Springer-Verlag, 2000, pp. 298–372. ISBN: 3-540-67973-1. URL: <http://dl.acm.org/citation.cfm?id=646271.685629>.
- [37] Jonsenser Zhao. "A new calculation for designing multilayer planar spiral inductors". In: *Edn -Boston then Denver then Highlands Ranch Co- 55* (July 2010), pp. 37–40.





## Acknowledgements

Desidero esprimere i miei più sentiti ringraziamenti a tutte le persone che hanno contribuito al completamento di questa tesi.

Innanzitutto, desidero ringraziare il mio relatore, il prof. Marcello Chiaberge, e corelatore, l'ing. Andrea Merlo, per avermi dato la possibilità di intraprendere questo progetto. Ringrazio l'ing. Marco Lapolla per la sua guida, disponibilità e dedizione nell'aiutarmi a sviluppare e perfezionare il mio lavoro.

Un ringraziamento speciale va alla mia famiglia che ha sempre sostenuto e incoraggiato il mio percorso accademico. Il loro sostegno e supporto sono stati la spinta necessaria per superare le sfide e raggiungere questo traguardo.

Ringrazio i compagni dell'università: Vale, Ali, Morgan, Matte, Nicoli, Franco, Luca e Nicco, che hanno alleviato le mie giornate e contro cui ho perso innumerevoli partite a bodriga.

Un ringraziamento agli amici di FORO, mia casa nell'ultimo periodo, con cui ho condiviso molte pause caffè.

Agli amici di una vita e compagni di mille avventure: Gian, Pier, Ale, Stol, Lollo e Chiara che, nonostante le nostre strade stiano prendendo direzioni diverse, sono e saranno sempre presenti al mio fianco.

Infine, il ringraziamento più importante va a Nau, mia compagna di viaggio, che mi ha sostenuto in questo percorso, credendo in me anche quando io non l'ho fatto.

Grazie mille a tutti.

*Fede*

